MAGLAB: A computing platform connecting geophysical signatures to melting processes in Earth's mantle

Malcolm Massuyeau, Emmanuel Gardés, Grégory Rogerie, Sonja Aulbach, Sebastian Tappe, Emmanuel Le Trong, David Sifré, Fabrice Gaillard

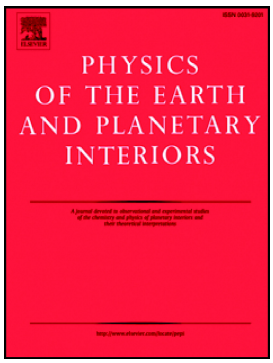

MAGLAB: A computing platform connecting geophysical signatures to melting processes in Earth's mantle

Malcolm Massuyeau, Emmanuel Gardés, Grégory Rogerie, Sonja Aulbach, Sebastian Tappe, Emmanuel Le Trong, David Sifré, Fabrice Gaillard

PII: S0031-9201(20)30398-8

DOI: https://doi.org/10.1016/j.pepi.2020.106638

Reference: PEPI 106638

To appear in: *Physics of the Earth and Planetary Interiors*

Received date: 7 July 2020

Revised date: 30 October 2020

Accepted date: 24 December 2020

Please cite this article as: M. Massuyeau, E. Gardés, G. Rogerie, et al., MAGLAB: A computing platform connecting geophysical signatures to melting processes in Earth's mantle, *Physics of the Earth and Planetary Interiors* (2020), https://doi.org/10.1016/j.pepi.2020.106638

MAGLAB: a computing platform connecting geophysical signatures to melting processes in Earth's mantle

Malcolm Massuyeau[1,2,†], Emmanuel Gardés[3], Grégory Rogerie[1], Sonja Aulbach[4], Sebastian Tappe[2], Emmanuel Le Trong[1], David Sifré[1,5], & Fabrice Gaillard[1]

[1]Institut des Sciences de la Terre d'Orléans (ISTO), Université d'Orléans-CNRS-BRGM, 1A rue de la Férollerie, 45071 Orléans cedex 2, France.

[2]Deep & Early Earth Processes (DEEP) Research Group, Department of Geology, University of Johannesburg, P.O. Box 524, Auckland Park 2006, South Africa.

[3]Centre de Recherche sur les Ions, les Matériaux et la Photonique (CIMAP), Normandie Université, ENSICAEN, UNICAEN, CEA, CNRS, Boulevard Henri Becquerel, BP 5133, F-14070 Caen cedex 5, France.

[4]Institut für Geowissenschaften, Goethe-Universität, Facheinheit Mineralogie, Abt. Petrologie und Geochemie, Altenhöferallee 1, D-60438 Frankfurt am Main, Germany.

[5]European Synchrotron Radiation Facility (ESRF), 71 avenue des Martyrs CS 40220, 38043 Grenoble Cedex 9, France.

Corresponding author: Malcolm Massuyeau (malcolm.massuyeau@wwu.de)

[†]present address: Institute for Mineralogy, University of Münster, Münster, Germany.

Keywords

Petrological-geophysical modeling; Melt fraction-composition; Upper mantle; CO_2-H_2O volatiles; Intraplate magmas; Lithosphere-asthenosphere boundary

Abstract

Decompression melting of the upper mantle produces magmas and volcanism at the Earth's surface. Experimental petrology demonstrates that the presence of CO_2 and H_2O enhances peridotite melting anywhere within the upper mantle down to approximately 200-300 km depth. The presence of mantle melts with compositions ranging from carbonate-rich to silicate-rich unavoidably affects the geophysical signals retrieved from Earth's mantle. Geochemical investigations of erupted intraplate magmas along with geophysical surveys allow for constraining the nature and volume of primary melts, and a sound formalism is required to integrate these diverse datasets into a realistic model for the upper mantle including melting processes. Here, we introduce MAGLAB, a model developed to calculate the composition and volume fraction of melts in the upper mantle, together with the corresponding electrical conductivity of partially molten mantle peridotites at realistic pressure-temperature conditions and volatile contents. We use MAGLAB to show how the compositions of intraplate magmas relate to variations in lithosphere thickness. Progressive partial melting of a homogeneous peridotitic mantle source can in theory create the diversity of compositions observed among the spectrum of intraplate magma types, with kimberlite melts beneath thick continental shields, alkaline magmas such as melilitite, nephelinite and basanite beneath thinner continents and relatively old plus thick oceanic lithospheres, and 'regular' basalts beneath the youngest and thinnest oceanic lithospheres as well as beneath significantly thinned continental lithospheres. MAGLAB calculations support recent experimental findings about the role of H_2O in the upper mantle on producing primary kimberlitic melts in addition to CO_2. We demonstrate the robustness of MAGLAB calculations by reproducing the compositions of erupted melts as well as associated mantle electrical conductivities beneath the Society hotspot in the Pacific Ocean. A comparison of our simulations with magnetotelluric surveys at various oceanic settings shows that the heterogeneities in electrical conductivity of Earth's upper mantle are related to variations in volatile content via the presence of small (generally <<1 wt%) and heterogeneously distributed fractions of CO_2-H_2O-bearing melts.

1. Introduction

The flux of heat from Earth's interior generates upwelling limbs of convective cells, such as passive upwelling beneath mid-ocean ridges, or plumes occurring beneath hotspots *(Ballmer et al., 2011; French and Romanowicz, 2015)*. Within these convective cells, the upper mantle is expected to produce partial melts of variable fractions and compositions. Mantle melting is enhanced by the presence of the volatiles CO_2 and H_2O. The upper mantle volatile contents average around 140 wt ppm CO_2 and 240 wt ppm H_2O *(Le Voyer et al., 2017)*, but are highly variable with concentrations ranging from some wt ppm to many hundreds of wt ppm as reported in geochemical surveys *(Marty, 2012; Le Voyer et al., 2017; Hirschmann, 2018; Hauri et al. 2019; Shimizu et al., 2019)*. Experimental petrology provides numerous constraints on partial melting properties of peridotite in presence of volatiles within the pressure-temperature-composition conditions prevailing in Earth's upper mantle. These studies emphasize the large effect of CO_2 and H_2O on mantle melting relations, where these volatiles drastically lower the solidus of peridotite to <1000 °C *(Wallace and Green, 1988; Dasgupta and Hirschmann, 2006; Hammouda and Keshav, 2013; Gardés et al., 2020)*. CO_2-H_2O-assisted melting is thus predicted for most of the upper mantle as long as the oxidized form of carbon (i.e. carbonate) is stable. The depth at which the transition from oxidized to reduced carbon occurs is debated, with options ranging from ~150 km *(Stagno et al., 2013)* to ~250 km *(Rohrbach and Schmidt, 2011)*. More recent studies *(Gaillard et al., 2015; Eguchi and Dasgupta, 2018; Moussallam et al., 2019)* argue that the asthenosphere may be much more oxidized than previously deduced from depleted peridotite samples of the deep cratonic lithosphere *(Stagno et al., 2013)*. Such deep cratonic mantle lithosphere may also have experienced various stages of metasomatism and oxidation over time by infiltrating carbonate-bearing hydrous silicate melts or by the incorporation of subducted carbonate-bearing crustal material *(Yaxley et al., 2017)*. The presence and role of volatile-bearing melts in both oceanic and continental upper mantle have been emphasized based on petrological investigations and geophysical observations. Geochemical studies have deduced their existence by observing characteristic metasomatic overprints of rocks as well as the presence of fluid/melt-derived inclusions in mantle minerals *(Bodinier et al., 1990; Grégoire et al., 2003; Klein-BenDavid et al., 2007; O'Reilly and Griffin, 2010; Weiss et al., 2011; Tumiati et al., 2013; Pilet et al., 2016)*. Seismic and magnetotelluric surveys have reported geophysical anomalies in the upper mantle, such as reduced seismic shear-wave velocities in the Low-Velocity Zone (LVZ) located between ~50 and 150-200 km depth, and high electrical conductivities at similar depths, both enhanced by the presence of low volumes of melt potentially containing appreciable amounts of CO_2 and H_2O *(Eggler, 1976; Gaillard et al., 2008; Kawakatsu et al., 2009; Fischer et al., 2010; Hirschmann, 2010; Ni et al., 2011; Schmerr, 2012; Naif et al., 2013; Sifré et al., 2014; Chantel et al., 2016; Holtzmann, 2016; Aulbach et al., 2017; Katsura et al., 2017; Kawakatsu and Utada, 2017; Tharimena et al., 2017a,b; Soltanmohammadi et al., 2018; Selway and O'Donnell, 2019; Selway et al., 2019; Rychert et al., 2020; Gardés et al., 2020)*. Interestingly, reworking, rejuvenation and ultimate loss of deep cratonic lithosphere sections (e.g., North Atlantic craton, North China craton, Tanzania craton) have been suggested to be an expression of intense metasomatic weakening due to repeated passage of volatile-bearing melts *(Tappe et al., 2007; Foley, 2008; Aulbach et al., 2017; Liu et al., 2019)*.

A wide range of magmatic liquids is stable in the upper mantle, ranging from carbonatites with low silica content at high pressures (i.e., great depths), to basanites-basalts with relatively high silica content at low pressures *(Gudfinnsson and Presnall, 2005; Dasgupta et al., 2013; Massuyeau et al., 2015)*. Indeed, near-solidus melts of peridotite in the

presence of CO_2 and H_2O are typically SiO_2-poor *(Foley et al., 2009)*, and decreasing pressure and increasing temperature increases the SiO_2 content of peridotite-derived melts *(Gudfinnsson and Presnall, 2005; Dasgupta et al., 2007, 2013; Massuyeau et al., 2015)*. The compositional diversity of mantle-derived melts is evidenced by the variability of intraplate magma compositions observed at the Earth's surface (Fig. 1). Some petrogenetic links have been established between the compositional diversity of mantle-derived magmas from oceanic (e.g., ocean island basalts (OIB)) to continental (e.g., kimberlite) intraplate settings and differences in the pressure of melt extraction from a compositionally similar upwelling mantle source *(le Roex, 1986; Ringwood et al., 1992; Gudfinnsson and Presnall, 2005; Tappe et al., 2013, 2018)*. On the other hand, geochemical studies have defined empirical relationships between the composition of basalts and the depth of melt extraction, i.e. the mean extent of melting, which is strongly controlled by lithospheric thickness *(Ellam, 1992; Haase, 1996; Prytulak and Elliott, 2007; Humphreys and Niu, 2009; Dasgupta et al., 2010; Niu et al., 2011; Davies et al., 2015; Niu and Green, 2018; Guo et al., 2020)*. Therefore, first-order variability in primitive basaltic melt compositions appears to relate to lithospheric thickness. However, a unifying model relating melt compositions in diverse tectonic settings, such as oceanic and continental intraplate magmatism, to lithospheric thickness is still lacking. Such a model requires describing chemical and physical properties of mantle melts by interpolating and extrapolating experimental data and comparing them with petrological and geophysical datasets for the terrestrial upper mantle. However, models calculating the compositions and fractions of melts equilibrated with peridotite in the presence of $CO_2 \pm H_2O$ are sparse *(Dasgupta et al., 2007, 2013; Hirschmann, 2010; Ghosh et al., 2014; Ghiorso and Gualda, 2015; Massuyeau et al., 2015)*. Importantly none of the existing models covers the whole compositional spectrum of mantle-derived melts equilibrated with peridotite within a large pressure-temperature (*P-T*) window, from carbonatitic to basaltic compositions, or allows for the calculation of both (i) composition and fraction of melt and (ii) corresponding geophysical response of partially molten mantle peridotite.

Here, we report on a new modeling platform, called MAGLAB (*http://calcul-isto.cnrs-orleans.fr/apps/maglab/*), which allows within a single framework to calculate (i) the compositions and fractions of melts equilibrated in the upper mantle as a function of its volatile content (CO_2 and H_2O) and (ii) corresponding electrical conductivities of partially molten peridotite under upper mantle conditions. MAGLAB covers most of the pressure-temperature-volatile conditions of the terrestrial upper mantle and reproduces the full spectrum of intraplate mantle-derived melts within their domain of stability, i.e. from carbonatitic and kimberlitic through to basanitic and basaltic compositions. This approach allows for simulating electrical conductivity profiles within a constrained petrological framework under relevant mantle conditions. The first part of this contribution presents the structure, formulations, and applicability of MAGLAB (Sections 2 and 3). Melt compositions, melt fractions and electrical conductivities of partially molten peridotite as a function of geodynamic setting are highlighted in Section 4. Based on our results, we demonstrate in Section 5, by using melt SiO_2 content as a first-order discriminant, that lithosphere thickness controls primary melt compositions. A diversity of intraplate magma compositions can be produced as a function of the depth of the lithosphere-asthenosphere boundary (LAB) even if only a single volume of upwelling mantle material is involved. The validity of MAGLAB model outputs for both melt fractions and compositions along with geophysical responses is then illustrated for a well-constrained intraplate setting, the Society hotspot in the Pacific Ocean. Section 5 furthermore shows the excellent match between the range of electrical conductivity simulated by MAGLAB for the Earth's upper mantle with realistic heterogeneities in CO_2-H_2O content and the heterogeneities in electrical conductivity of the oceanic upper mantle reported from magnetotelluric surveys.

2. The MAGLAB model

MAGLAB aims at calculating the composition and the fraction of melt in chemical equilibrium with mantle peridotite at a given pressure, temperature and bulk rock CO_2 and H_2O content. As detailed in following sections, MAGLAB calculates melt compositions in the system SiO_2-TiO_2-Al_2O_3-FeO-CaO-MgO-Na_2O-K_2O-H_2O-CO_2, based on the silica activity of the melt (i.e., how ideal is the mixing between silica and other melt components). Silica activity is calculated at given *P-T* conditions and olivine-orthopyroxene compositions, and three compositional end-members (silicate, carbonate, H_2O) are mixed in order to determine the melt composition that reproduces this activity best. At a given bulk rock CO_2 and H_2O content, the melt fraction is obtained by mass balance using the CO_2 and H_2O concentrations of the melt and volatile partitioning between melt and peridotite. Once melt composition and melt fraction have been determined, MAGLAB calculates the electrical conductivity of corresponding partially molten mantle peridotite.

2.1. Calculation of melt composition and fraction at upper mantle conditions

The MAGLAB model first calculates melt composition and melt fraction at given pressure, temperature and bulk rock CO_2 and H_2O content. The compositions of CO_2-H_2O-bearing melts in pressure-temperature-bulk rock composition space are calculated according to a thermodynamic model modified after *Massuyeau et al. (2015)*. The melt-mantle rock equilibrium is simplified according to the reaction

$$Mg_2SiO_4 + SiO_2(melt) = Mg_2Si_2O_6 \quad (1)$$

where Mg_2SiO_4 is the forsterite component of olivine, $Mg_2Si_2O_6$ is the enstatite component of orthopyroxene, and SiO_2 (melt) is the silica component of melt. Equilibrium implies

$$\Delta G^* + RT\,ln\left(\frac{a_{Mg_2Si_2O_6}^{Orthopyroxene}}{a_{SiO_2}^{Melt,1}\,a_{Mg_2SiO_4}^{Olivine}}\right) = 0,$$

$$\text{or } a_{SiO_2}^{Melt,1} = exp\left(\frac{\Delta G^*}{RT}\right)\left(\frac{a_{Mg_2Si_2O_6}^{Orthopyroxene}}{a_{Mg_2SiO_4}^{Olivine}}\right), \quad (2)$$

where ΔG^* is the standard state Gibbs free energy of reaction (1), a_i^j is the activity of component i in phase j, R is the gas constant and T the absolute temperature. At given P and T, $a_{SiO_2}^{Melt,1}$ is obtained by calculating ΔG^* according to the data of *Holland and Powell (2011)* (Section 1 of the Supplementary Information). Mineral activities are given by $a_{Mg_2SiO_4}^{Olivine} = X_{Mg}^{M1,Olivine} X_{Mg}^{M2,Olivine}$ and $a_{Mg_2Si_2O_6}^{Orthopyroxene} = X_{Mg}^{M1,Orthopyroxene} X_{Mg}^{M2,Orthopyroxene}$, where $X_{Mg}^{M1,Olivine}$ and $X_{Mg}^{M2,Olivine}$ are the mole fraction of Mg in the M1 site and the M2 site of olivine, respectively, and $X_{Mg}^{M1,Orthopyroxene}$ and $X_{Mg}^{M2,Orthopyroxene}$ are the mole fraction of Mg in the M1 site and the M2 site of orthopyroxene, respectively (see more details about calculations of mineral activities in *Massuyeau et al. (2015)*). SiO_2 mixing in melt is not

considered ideal. *Massuyeau et al. (2015)* found that the activity coefficient of SiO_2 in the melt, $\gamma_{SiO_2}^{Melt}$, which describes the deviation from ideal behavior of the mixing between SiO_2 and other components *(DeCapitani and Kirschen, 1998)*, is well modeled in the SiO_2-TiO_2-Al_2O_3-FeO-CaO-MgO-Na_2O-K_2O-H_2O-CO_2 space as:

$$RT\,ln\left(\gamma_{SiO_2}^{Melt}\right) = W_{SiO_2-CO_2}^{a}\left(2X_{SiO_2}^{Melt}X_{CO_2}^{Melt} - 2\left(X_{SiO_2}^{Melt}\right)^2X_{CO_2}^{Melt}\right) + \left(W_{SiO_2-CO_2}^{b} + +PW_{SiO_2-CO_2}^{c}\right)\left(\left(X_{CO_2}^{Melt}\right)^2 - 2X_{SiO_2}^{Melt}\left(X_{CO_2}^{Melt}\right)^2\right) + W_{Al_2O_3-SiO_2}\,X_{Al_2O_3}^{Melt}\left(1 - X_{SiO_2}^{Melt}\right) + W_{CaO-SiO_2}\,X_{CaO}^{Melt}\left(1 - X_{SiO_2}^{Melt}\right) + W_{Na_2O-SiO_2}\,X_{Na_2O}^{Melt}\left(1 - X_{SiO_2}^{Melt}\right) + W_{K_2O-SiO_2}\,X_{K_2O}^{Melt}\left(1 - X_{SiO_2}^{Melt}\right) - W_{Al_2O_3-CO_2}\,X_{Al_2O_3}^{Melt}X_{CO_2}^{Melt} - W_{FeO-CO_2}\,X_{FeO}^{Melt}\,X_{CO_2}^{Melt} - W_{MgO-CO_2}\,X_{MgO}^{Melt}X_{CO_2}^{Melt} - W_{Na_2O-CO_2}\,X_{Na_2O}^{Melt}X_{CO_2}^{Melt} - W_{K_2O-CO_2}\,X_{K_2O}^{Melt}\,X_{CO_2}^{Melt} - W_{H_2O-CO_2}X_{H_2O}^{Melt}X_{CO_2}^{Melt} - W_{Al_2O_3-FeO}\,X_{Al_2O_3}^{Melt}X_{FeO}^{Melt} - W_{Al_2O_3-MgO}\,X_{Al_2O_3}^{Melt}X_{MgO}^{Melt} - W_{FeO-CaO}\,X_{FeO}^{Melt}X_{CaO}^{Melt} - W_{CaO-Na_2O}\,X_{CaO}^{Melt}X_{Na_2O}^{Melt}, \quad (3)$$

where the pressure P is expressed in bar, X_i^{Melt} is the molar fraction of oxide i in melt and the W_{i-j} are the Margules parameters, i.e. the interaction parameters between two melt oxides i and j. Noteworthy, Eq. (3) is modified from *Massuyeau et al. (2015)* by the addition of a pressure-dependent Margules parameter $W_{SiO_2-CO_2}^{c}$ for the interaction SiO_2-CO_2. This term was added since it allows for a better reproduction of the progressive transition between carbonate-rich to silicate-rich melts with pressure (see details in Section 3; *Stagno and Frost, 2010; Dasgupta et al., 2013; Massuyeau et al., 2015*). The activity of SiO_2 in the melt can then be calculated from Eq. (3) according to

$$a_{SiO_2}^{Melt,2} = X_{SiO_2}^{Melt}\gamma_{SiO_2}^{Melt}. \quad (4)$$

The Margules parameters in Eq. (3) are optimized so that $a_{SiO_2}^{Melt,2}$ calculated from experimental melt compositions following Eq. (4) best reproduces $a_{SiO_2}^{Melt,1}$ calculated from experimental P and T following Eq. (2) (Tables S1-S2; more details about the calculations and the optimization procedure can be found in *Massuyeau et al. (2015)*). The optimization was done over an extended experimental database covering a large range of pressure, temperature and composition conditions relevant to the upper mantle. It regroups 678 melting experiments at pressures and temperatures ranging from 1 to 14 GPa and 1020 to 1950°C, and bulk rock CO_2 and H_2O contents from 0 to 10 – 20 wt% (Fig. 2A; see also Table S3). This corresponds to 187 more entries than in *Massuyeau et al. (2015)*. MAGLAB reproduces experimental data to within ~15% based on the average relative deviation of MAGLAB calculations for the whole database (Fig. 3).

Once the Margules parameters are optimized over the experimental database, MAGLAB can be used to calculate mantle-derived melt compositions at any P and T. First, the activity of SiO_2 in the melt $a_{SiO_2}^{Melt,1}$ is calculated from Eq. (2) at P and T of interest, assuming a pressure-dependent activity ratio $\frac{a_{Mg_2Si_2O_6}^{Orthopyroxene}}{a_{Mg_2SiO_4}^{Olivine}}$ for the upper mantle estimated from experimental data (Fig. S1; see details in Section 2 of the Supplementary Information). Then, the method consists in finding the composition for which the SiO_2 activity $a_{SiO_2}^{Melt,2}$ calculated from Eq. (4) matches the SiO_2 activity $a_{SiO_2}^{Melt,1}$ calculated from Eq. (2) (see Fig. S2). However,

instead of searching for a solution in the whole SiO_2-TiO_2-Al_2O_3-FeO-CaO-MgO-Na_2O-K_2O-H_2O-CO_2 compositional space, we designed MAGLAB to work in the space of three end-members: silicate (S), carbonate (C) and H_2O (H). The melt composition is thus calculated as a linear combination of the three end-members, i.e. $\alpha S + \beta C + \varepsilon H$, where the coefficients α, β and ε are optimized for minimizing the difference between $a_{SiO_2}^{Melt,1}$ and $a_{SiO_2}^{Melt,2}$ (with α, β and ε being all positive and such that $\alpha + \beta + \varepsilon = 1$). The use of these three end-members reduces the degrees of freedom but their compositions were defined in a way that their combination covers most of the compositional range of both experimental and natural melts (Figs 2B-S3). This procedure allows for reproducing a wide range of natural volatile-bearing melts produced in equilibrium with peridotite, from carbonatites to kimberlites to basanites and basalts. Strongly alkaline magmas and intrusive carbonatites, as well as some kimberlites and basalts, may require additional differentiation processes or the involvement of other lithologies such as eclogite, pyroxenite or hornblendite, which are not treated by the present model *(Hirschmann et al., 2003; Sobolev et al., 2007; Pilet et al., 2008; Doucelance et al., 2010; Baudouin et al., 2016; Tappe et al., 2017; Weidendorfer et al., 2017; Lu et al., 2020)*. Note that the compositions of the silicate and carbonate melt end-members are not constant but vary as a function of pressure (Fig. S4 and Table S4). Moreover, the pure H_2O end-member allows water content to vary independently from CO_2 content, contrary to the model of *Massuyeau et al. (2015)*. Details on calculations and compositions of the melt end-members are provided in Section 3 of the Supplementary Information.

In addition to melt composition, melt fraction can also be determined using volatile partitioning. CO_2 is treated as highly incompatible, i.e. entirely residing in the melt (e.g. *Dasgupta et al., 2013*). The H_2O content of the melt is constrained using partition coefficients for nominally anhydrous minerals/hydrous silicate melt systems from *Hirschmann et al. (2009)* and *Novella et al. (2014)*. Note that H_2O solubility does not significantly differ between CO_2-poor basaltic melts and CO_2-rich, low-SiO_2 melts *(Dasgupta et al., 2013; Moussallam et al., 2016)*. Thus, the mass fraction of melt, F_m^{Melt}, can be calculated either from CO_2 partitioning

$$F_m^{Melt,1} = \frac{C_{CO_2}^{Bulk}}{C_{CO_2}^{Melt}}, \quad (5)$$

or from H_2O partitioning

$$F_m^{Melt,2} = \frac{\frac{C_{H_2O}^{Bulk}}{C_{H_2O}^{Melt}} - D_{H_2O}^{Peridotite/Melt}}{1 - D_{H_2O}^{Peridotite/Melt}}. \quad (6)$$

$C_{CO_2}^{Bulk}$ and $C_{H_2O}^{Bulk}$ are the mass fractions of CO_2 and H_2O in bulk peridotite rock in wt%, respectively. $C_{CO_2}^{Melt}$ and $C_{H_2O}^{Melt}$ are the mass fractions of CO_2 and H_2O in melt in wt%, respectively, converted from the molar fractions $X_{CO_2}^{Melt}$ and $X_{H_2O}^{Melt}$ calculated above. $D_{H_2O}^{Peridotite/Melt}$ is the pressure-dependent partition coefficient of H_2O between peridotite and melt, calculated as follows:

$$D_{H_2O}^{Peridotite/Melt} = X_{Ol} D_{H_2O}^{Ol/Melt} + X_{Opx} D_{H_2O}^{Opx/melt} + X_{Cpx} D_{H_2O}^{Cpx/Melt} + X_{Grt} D_{H_2O}^{Grt/melt} + X_{Sp} D_{H_2O}^{Sp/Melt}, \quad (7)$$

where X_{Ol}, X_{Opx}, X_{Cpx}, X_{Grt} and X_{Sp} are the modal proportions of olivine, orthopyroxene, clinopyroxene, garnet and spinel, respectively, calculated from *Hirschmann et al. (2009)*, and $D_{H_2O}^{Ol/Melt}$, $D_{H_2O}^{Opx/Melt}$, $D_{H_2O}^{Cpx/Melt}$, $D_{H_2O}^{Grt/Melt}$ and $D_{H_2O}^{Sp/Melt}$ are the partition coefficients of H_2O of olivine, orthopyroxene, clinopyroxene, garnet and spinel, respectively, in equilibrium with melt, calculated from *Hirschmann et al. (2009)* and *Novella et al. (2014)* (see details in Section 4 of the Supplementary Information). Hence, two different melt fractions can be obtained when varying $C_{CO_2}^{Melt}$ and $C_{H_2O}^{Melt}$ independently following Eqs. (5) and (6), which should converge to an identical value. The optimizations of melt composition and melt fraction are thus performed concomitantly in such a way that $\left(a_{SiO_2}^{Melt,1} - a_{SiO_2}^{Melt,2}\right)^2 + 100\left(F_m^{Melt,1} - F_m^{Melt,2}\right)^2$(8) is minimized (see details about the optimization procedure in Section 5 of the Supplementary Information).

For some pressure-temperature-bulk rock composition conditions, melt composition cannot be unequivocally predicted and MAGLAB yields two distinct solutions, carbonate-rich and silicate-rich. This numerical feature, which relies on the Margules formalism used to calculate $a_{SiO_2}^{Melt,1}$ in Eq. (2), occurs mainly at low *P-T* conditions and for H_2O-poor peridotite systems. It is indicative of the non-ideality in the mixing between silicate and carbonate components at these conditions, which ultimately results in immiscibility *(Dasgupta et al., 2013; Massuyeau et al., 2015)*. However, we expect only one liquid to be stabilized because immiscibility is not reported in most of the experimental studies of melting in peridotitic compositions *(Martin and Schmidt, 2013; Hammouda and Keshav, 2015)*. Since silicate-rich melts are favored at high *T* and low *P* and, conversely, carbonate-rich melts are favored at low *T* and high *P*, we use a pressure-dependent formulation to determine, at a given *P*, the most probable stable melt composition between these two distinct compositional solutions as a function of *T* (Fig. S5).

2.2. Calculation of the electrical conductivity for model mantle peridotite

The second part of MAGLAB calculates the bulk electrical properties of mantle rocks with melt composition and melt fraction equilibrated at P, T and bulk rock CO_2 and H_2O content. As volatile-bearing melts interconnect in mantle rocks at any melt fraction *(Gardés et al., 2020)*, the bulk electrical conductivity of partially molten mantle peridotite is a combination of the conductivity of the rock and the conductivity of the melt weighted by melt fraction.

The electrical conductivity of melt is calculated following the model of *Sifré et al. (2014, 2015)* for CO_2- and H_2O-bearing melts

$$\sigma_{melt} = \sigma^{H_2O} + \sigma^{CO_2} = \sigma_0^{H_2O} exp\left(\frac{-\left(E_a^{H_2O} + 0.2(P-30000)\right)}{RT}\right) + \sigma_0^{CO_2} exp\left(\frac{-\left(E_a^{CO_2} + 0.2(P-30000)\right)}{RT}\right), \quad (9)$$

where P is the pressure (bar), and σ_0 and E_A are the pre-exponential factor (S m^{-1}) and the activation energy (J mol^{-1}), respectively, for the two Arrhenius laws describing the contributions of the hydrous silicate component (σ^{H_2O}) and the carbonate component (σ^{CO_2})

$$ln\left(\sigma_0^{H_2O}\right) = 4.54\,10^{-5}\,E_a^{H_2O} + 5.5607 \text{ with } E_a^{H_2O} = 88774\,exp\left(-0.3880\,C_{H_2O}^{Melt}\right) + 73029, \quad (10)$$

and $ln\left(\sigma_0^{CO_2}\right) = 5.50\,10^{-5}\,E_a^{CO_2} + 5.7956$ with $E_a^{CO_2} = 789166\,exp\left(-0.1808\,C_{CO_2}^{Melt}\right) + 32820$. (11)

This law is valid for $C_{CO_2}^{Melt}$ from 0 to ~50 wt% and $C_{H_2O}^{Melt}$ from 0 to ~10 wt%.

The electrical conductivity of the solid rock is assumed to be controlled by the conductivity of olivine. We use the model of *Gardés et al. (2014)* which provides conductivity as a function of temperature and H_2O content

$$\sigma_{ol} = 10^{5.07} exp\left(-\frac{239000}{RT}\right) + 10^{2.34} exp\left(-\frac{144000}{RT}\right) + 10^{-1.17}\left(10000\,C_{H_2O}^{Olivine}\right) exp\left(-\frac{89000 - 2080\left(10000\,C_{H_2O}^{Olivine}\right)^{1/3}}{RT}\right). \quad (12)$$

$C_{H_2O}^{Olivine}$, the mass fraction of water in olivine in wt%, is given by

$$C_{H_2O}^{Olivine} = C_{H_2O}^{Melt} D_{H_2O}^{Ol/Melt}, \quad (13)$$

where $D_{H_2O}^{Ol/Melt}$ is the partition coefficient of H_2O between olivine and melt (see Section 4 of the Supplementary Information).

Following *Sifré et al. (2014)*, the mixing model for calculating the bulk conductivity of partially molten mantle peridotite is taken as a combination of an Hashin-Shtrikman upper bound (HS+) mixing model and a tube mixing model (e.g. *Schmeling, 1986*)

$$\sigma_{bulk} = \frac{1}{2}\left(\left(\frac{F_v^{Melt}}{\sigma_{melt}+2\sigma_{melt}} + \frac{\left(1-F_v^{Melt}\right)}{\sigma_{ol}+2\sigma_{melt}}\right)^{-1} - 2\sigma_{melt}\right) + \frac{1}{2}\left(\frac{1}{3}F_v^{Melt}\sigma_{melt} + \left(1-F_v^{Melt}\right)\sigma_{ol}\right), \quad (14)$$

where the volume fraction of melt F_v^{Melt} is given by

$$F_v^{Melt} = \frac{\left(\frac{F_m^{Melt}}{d_{melt}}\right)}{\left(\frac{F_m^{Melt}}{d_{melt}} + \frac{\left(1-F_m^{Melt}\right)}{d_{olivine}}\right)}. \quad (15)$$

Olivine density $d_{olivine}$ is taken as 3.34 (average of values given for olivine in both spinel and garnet peridotite in Table 1a of *Lee (2003)*). Following *Sifre et al. (2014)*, melt density d_{melt} is calculated as

$$d_{melt} = \frac{C_{H_2O}^{Melt}}{100} d_{H_2O} + \frac{2C_{CO_2}^{Melt}}{100} d_{CO_2} + \left(1 - \frac{C_{H_2O}^{Melt}+2C_{CO_2}^{Melt}}{100}\right) d_{basalt} \quad (16)$$

with $d_{H_2O} = 1.4$, $d_{CO_2} = 2.4$, and $d_{basalt} = 2.8$.

3. MAGLAB: comparison with previous models

In contrast to models developed for dry and hydrous silicate magmatic systems (e.g., MELTS family: *Ghiorso and Sack (1995)*, *Ghiorso et al. (2002)*, *Gualda et al. (2012)*; COMAGMAT: *Ariskin (1999)*; PerpleX: *Connolly (2005)*), only a few models allow for calculating the composition and fraction of melts derived from peridotite melting in the presence of CO_2 and H_2O, and their range of applicability is limited, especially in terms of composition and pressure. The model of *Ghiorso and Gualda (2015)* addresses silicate melts with limited dissolved CO_2 and H_2O components and is not relevant to investigating carbonate-rich melts with CO_2 content >~10 wt% or P > 3 GPa. Calculation of melt composition is limited to CO_2, H_2O and SiO_2 oxides in the model of *Dasgupta et al. (2013)*, CO_2 and H_2O in the model of *Hirschmann (2010)*, and to CO_2 only in the models of *Dasgupta et al. (2007)* and *Ghosh et al. (2014)*. Furthermore, the pressure range of application is ≤5 GPa for the models of *Dasgupta et al. (2007, 2013)*, *Hirschmann (2010)* and *Ghiorso and Gualda (2015)*, and >10 GPa for the model of *Ghosh et al. (2014)*. Thus, none of these models allows calculations at pressures between 5 and 10 GPa. The model of *Massuyeau et al. (2015)* does not allow varying bulk rock CO_2 and H_2O contents independently. To date, MAGLAB is the model simulating the widest ranges of temperature and pressure, from ~900 to 1700°C and from ~2 to 10 GPa (i.e., from ~60 to 300 km depth). It allows composition calculations in SiO_2-TiO_2-Al_2O_3-FeO-CaO-MgO-Na_2O-K_2O-H_2O-CO_2 space where, notably, CO_2 and H_2O are independent variables.

A key feature of mantle-relevant melting is the abrupt transition from carbonatitic melts (<15 wt% SiO_2) to silicate-rich melts (>30 wt% SiO_2), as illustrated by experimental data at e.g. 3 and 5 GPa where the transition occurs at ~1350°C and ~1450°C respectively (Fig. 4A-B). At 3 and 5 GPa, both *Dasgupta et al. (2007)* and *Dasgupta et al. (2013)* do not reproduce this abrupt transition. At 5 GPa, the model of *Dasgupta et al (2013)* yields an almost linear positive evolution of the SiO_2 content with increasing temperature corresponding to a near ideal system. At 3 GPa, the model of *Dasgupta et al. (2007)* fails to predict the formation of carbonatite melts at low temperatures (Fig. 4A). On the other hand, MAGLAB captures this chemical shift at 3 and 5 GPa, as does the model of *Massuyeau et al. (2015)* (Fig. 4A-B). In contrast, MAGLAB produces a smoother transition from carbonate-rich melts to silicate-rich melts at higher pressures, as observed experimentally at e.g. 7 and 10 GPa, which is not well captured in the model of *Massuyeau et al. (2015)* (Fig. 4C-D).

Thus, MAGLAB fairly well reproduces the wide range of mantle-relevant, CO_2±H_2O-bearing melts. It applies to pressures and temperatures covering most of Earth's upper mantle regions subject to (CO_2+H_2O)-assisted melting *(Wallace and Green, 1988; Foley et al., 2009)* which, away from ridges, starts at depths >~60 km beneath mature to old oceanic lithosphere (Fig. 5). Moreover, in addition to melt composition, MAGLAB also allows the calculation of melt fraction and corresponding bulk rock electrical conductivity. It should be noted, however, that MAGLAB calculations are valid as long as oxygen fugacity stabilizes carbonates as important carbon species, i.e. in upper mantle regions, estimated between ~60 km and ~300 km depth *(Wallace and Green, 1988; Hirschmann, 2010; Rohrbach and Schmidt, 2011; Stagno et al., 2013; Gaillard et al., 2015; Yaxley et al., 2017; Dasgupta, 2018; Eguchi and Dasgupta, 2018; Moussallam et al., 2019; Gardés et al., 2020)*. Furthermore, calculations are not possible at zero bulk rock CO_2 content and in a set of extreme *P-T*-volatile content conditions, e.g. at low *P* <5 GPa in very hot mantle with potential temperature T_P >1500-1600°C, or even at higher pressures for bulk rock CO_2-H_2O contents >0.1-0.2 wt% and with H_2O/CO_2 molar ratio >10-20 (see details in Section 6 of the

Supplementary Information; MAGLAB hyperlink: *http://calcul-isto.cnrs-orleans.fr/apps/maglab/).*

4. MAGLAB simulations of oceanic and cratonic mantle

We used MAGLAB to calculate melt composition, melt fraction and associated electrical conductivity of the upper mantle in oceanic and cratonic settings, with focus on three main parameters: lithospheric thickness, mantle potential temperature (T_P), and mantle CO_2-H_2O content. It should be noticed that the following results correspond to equilibrium melt fractions and compositions, and thus do not consider dynamic phenomena such as melt migration, melt accumulation and depletion processes. The position of the base of the lithosphere, i.e. LAB depth, can be approximately located within the thermal boundary layer where a time-dependent thermal transition from the conductive to fully convecting upper mantle occurs *(Parsons and McKenzie, 1978; McKenzie and Bickle, 1988; Jaupart and Mareschal, 1999; McKenzie et al., 2005; An et al., 2015; Priestley et al., 2019)*. It is hereafter defined at the base of this thermal boundary layer *(Jaupart and Mareschal, 1999; An et al., 2015)* as the depth where mantle temperature is lowered by 10°C from the temperature of the adiabatic geotherm. Although we acknowledge that our definition for identifying the base of the lithosphere is somewhat simplistic in comparison with the complex and diffuse nature of the lithosphere-asthenosphere transition, this method provides a reasonable estimation of the lithospheric thickness, with the advantage of being consistent when applied to different tectonic settings.

Fig. 5 reports MAGLAB simulations for an ambient oceanic upper mantle with average volatile content, i.e. 140 wt ppm CO_2 – 240 wt ppm H_2O *(Le Voyer et al., 2017)*, and a potential temperature T_P of 1350°C (thermal model G13R1350 from *Grose and Afonso (2013)*). The most striking result is the contrast in melt composition and melt fraction between the asthenosphere and the lithosphere.

In the asthenosphere, from high to low pressure, both melt SiO_2 content and melt fraction increase while melt CO_2 content and bulk electrical conductivity decrease. The evolution of melt composition is consistent with the increase in silica activity with decreasing pressure *(Carmichael et al., 1970; Massuyeau et al., 2015)*, as well as with the systematic complementarity of melt CO_2 content and melt SiO_2 content observed experimentally (e.g. *Gudfinnsson and Presnall, 2005, Dasgupta et al., 2007, 2013; Ghosh et al., 2014*). At around 300 km depth, a fraction of ~0.05 wt% (0.06 vol.%) of carbonatitic melt is produced, with SiO_2, CO_2 and H_2O contents of ~11, 31 and 4 wt%, respectively, and mantle electrical conductivity σ_{bulk} is about $10^{-0.9}$ S m^{-1}. At 80 km depth beneath ridges to young lithospheres (<~10 Ma), a fraction of 0.24 wt% (0.30 vol%) of silicate-rich melt is produced, with SiO_2, CO_2 and H_2O contents of ~42, 6 and 2 wt%, respectively, and σ_{bulk} is ~$10^{-1.4}$ S m^{-1}. Noteworthy, for constant volatile content in the source, variations reported in mantle electrical conductivity are buffered by the opposite effects of melt composition and melt fraction: for example, volatile contents increase σ_{bulk}, but smaller melt fractions decrease it.

The evolution strongly differs beneath mature to old lithospheres (>~50 Ma), where both melt SiO_2 content and melt fraction drop while melt CO_2 content rises in the lithosphere. These abrupt changes in melt composition and melt fraction from asthenosphere to lithosphere are a direct consequence of the abrupt change in temperature (Fig. 4), and may be accompanied by a slight increase in bulk electrical conductivity (e.g., near LAB depth at 120-125 km in an ambient oceanic upper mantle with average volatile content; see profile "Ambient" in Fig. 6F). At 80 km depth in 70 Ma oceanic lithosphere, a fraction of 0.03 wt% (0.05 vol%) of carbonatitic melt is produced, with SiO_2, CO_2 and H_2O contents of ~2, 42 and 2.5 wt%, respectively, and σ_{bulk} is about $10^{-1.45}$ S m^{-1}. Note that melting stops when crossing the CO_2-H_2O-bearing peridotite solidus above 60-70 km depth beneath mature to old

lithospheres (P <~2 GPa and T <~930-1100°C; grey areas in Fig. 5, see also Fig. 2). Then, mantle electrical conductivity is mainly controlled by olivine, with values $<10^{-2}$ S m^{-1} *(Gardés et al., 2014)*.

The base of mature to old lithospheres thus corresponds to a region where melt fraction is maximum. At the vicinity of the LAB beneath >~50 Ma lithospheres, i.e. at 120-125 km depth, a fraction of 0.14 wt% (0.17 vol%) of silicate-rich melt is present, with SiO_2, CO_2 and H_2O contents of ~35, 10 and 3 wt%, respectively, and mantle electrical conductivity σ_{bulk} is about $10^{-1.2}$ S m^{-1}.

Melt composition, melt fraction and mantle electrical conductivity profiles in 70 Ma oceanic lithosphere for various T_P and volatile contents are reported in Figs 6 and 7, respectively. In Fig. 6, we report calculations for a mantle with average volatile content and various T_P of 1300, 1350, 1400 and 1450°C (G13R1300, G13R1350, G13R1400 and G13R1450 models from *Grose and Afonso (2013)*), corresponding to cold, ambient, hot, and hotspot settings, respectively. Near the LAB, at ~115-125 km depth, MAGLAB yields melt compositions ranging from ~7 to 40 wt% SiO_2, 37 to 5 wt% CO_2 and 4 to 3 wt% H_2O from cold mantle (~1350°C at LAB depth) to hotspot-like mantle (~1500°C at LAB depth), respectively (Fig. 6A-D). Melt fraction ranges between 0.04 and 0.26 wt% (0.05-0.32 vol%) within the same temperature interval (Fig. 6E), while σ_{bulk} slightly increases from $10^{-1.15}$ to $10^{-1.06}$ S m^{-1} approximately (Fig. 6F). Note that most of the variations in composition and melt fraction occurs between cold and ambient settings since, e.g., the range of SiO_2 content reduces to 35-40 wt% from ambient to hotspot settings. The electrical conductivity remains, however, rather constant because the large variation in melt composition, changing from silicate-rich in hotspot settings to carbonatitic in cold settings, is compensated by a large decrease in melt fraction.

In Fig. 7, mantle CO_2 and H_2O contents are varied around their average contents in an ambient mantle: 50 – 80, 140 – 240 and 420 – 720 wt ppm CO_2 – wt ppm H_2O, corresponding to depleted, average, and enriched mantle source, respectively. Near LAB depth, depleted to enriched sources produce silicate-rich melts with an almost constant melt SiO_2 content of around 35 wt%, a slightly variable melt CO_2 content ranging from 11 to 8 wt%, and a more variable melt H_2O content spanning the range 1-6 wt%, respectively (Fig. 7B-D). On the other hand, melt fraction dramatically increases from about 0.04 to 0.54 wt% (~0.05-0.68 vol%) from depleted to enriched sources, respectively, illustrating the strong dependence of melt fraction on volatile content (Fig. 7E). As a consequence, contrary to temperature variations, the large increase in melt fraction together with variations in melt volatile content from depleted to enriched volatile content induce a large variation in electrical conductivity, from $10^{-1.54}$ to $10^{-0.76}$ S m^{-1} (Fig. 7F).

Importantly, at any of the temperature and bulk rock volatile content simulated, no transitional melts with intermediate compositions between silicate-rich and carbonatitic melt, i.e. carbonated silicate melts with SiO_2 content within the range 15-35 wt%, are obtained near the LAB in oceanic mantle. In contrast, the asthenosphere beneath extremely thick continental lithosphere, such as in undisturbed cratonic regions, can give rise to melts with low to intermediate SiO_2 contents at realistic pressure-temperature-volatile content conditions (Fig. 8B). We performed MAGLAB calculations along a typical cratonic geotherm, with T_P = 1350°C and considering various bulk rock volatile contents as previously described (see details about geotherm in Figs 8A-S6 and their caption). Near the LAB, at ~210 km depth, while depleted to average mantle sources produce carbonatitic melts with <~15 wt% SiO_2, >~30 wt% CO_2 and <~5 wt% H_2O, enriched sources produce kimberlitic melt with intermediate SiO_2 and CO_2 contents of ~22 and ~18 wt%, respectively, and an H_2O content of

about 9 wt% (Fig. 8B-D). Noteworthy, similar kimberlitic, transitional melts are calculated in the case of a CO_2-average and H_2O-enriched mantle (i.e., with 140 wt ppm CO_2 – 720 wt ppm H_2O; Fig. 8B). As with oceanic mantle, melt fraction at LAB depth beneath cratonic settings largely increases from depleted to enriched sources, from ~0.01 to 0.24 wt% (0.02-0.31 vol%), which, coupled with variations in melt volatile content, induces a large increase in electrical conductivity, from about $10^{-1.4}$ to $10^{-0.5}$ S m^{-1} (Fig. 8E-F).

5. Discussion

5.1. Linking the diversity of mantle-sourced intraplate magmatism to lithosphere thickness

The composition of intraplate magmas generally relates to the tectonic setting in which they were produced, with mid-ocean ridge basalts (MORB) sampled around oceanic ridges, OIBs mainly erupted over ocean floors away from plate boundaries, and kimberlites quasi-exclusively observed on continental shields, mainly on-craton. These systematics indicate that geodynamic context exerts a primary control on the compositional spectrum of intraplate magmatism. One of the main features varying between different tectonic settings is lithosphere thickness, being thin near oceanic ridges and thick beneath most cratons. It is therefore reasonable to assume that variations in lithosphere thickness may generate variations in primitive melt composition, without invoking large compositional variations in the mantle sources *(le Roex, 1986; Ringwood et al., 1992; Gudfinnsson and Presnall, 2005; Tappe et al., 2013, 2016, 2018; Grose and Afonso, 2019; Baudouin and Parat, 2020)*. A critical effect of lithosphere thickness on the composition of mantle-derived intraplate alkaline basalts and basalts (i.e., melts with >40 wt% SiO_2) has been outlined in previous geochemical studies: with increasing lithospheric thickness, the final equilibrium pressure before melt extraction increases, lowering the degree of melting and thus lowering melt SiO_2 and Al_2O_3 contents, while increasing MgO and FeO contents *(Haase, 1996; Humphreys and Niu, 2009; Dasgupta et al., 2010; Niu et al., 2011; Davies et al., 2015; Zhang et al., 2017; Guo et al., 2020)*. Furthermore, a natural example for the continuum of melt composition ranging from kimberlitic to OIB-type alkaline basaltic was described in *Tappe et al. (2007)*, where changes in magma composition through time are explained as a function of significant lithosphere thinning of a single cratonic block. Excluded from this concept are lamproites and other highly potassic magma types, as well as intrusive carbonatites, because these intraplate magmas have typically experienced variable contributions from strongly metasomatized non-peridotitic components of the mantle lithosphere, or they can be highly differentiated in nature *(Becker and le Roex, 2006; Pilet et al., 2008; Doucelance et al., 2010; Weidendorfer et al., 2017; Tappe et al., 2017)*.

Here, we use MAGLAB to simulate the effect of varying lithosphere thickness on primitive melt composition by calculating volatile-bearing melt compositions in equilibrium with peridotite near the LAB and comparing them with corresponding erupted magmas. We performed MAGLAB simulations by varying LAB depth as a function of the tectonic setting (see *P-T* conditions in Fig. S7), and considering a single homogeneous mantle source with 140 wt ppm CO_2 and 240 wt ppm H_2O on average *(Le Voyer et al., 2017)*. Using the SiO_2 content as a relevant proxy for the compositional variability of intraplate magmatism in Fig. 9, the composition of erupted basaltic magmas such as MORBs and OIBs with SiO_2 >45 wt% are well reproduced by MAGLAB beneath the thinnest and youngest oceanic lithospheres with LAB depths <60 km. Primitive alkaline magmas such as melilitites, nephelinites, basanites and silica-poor OIBs with 35-45 wt% SiO_2 are reproduced by MAGLAB beneath the thickest oceanic lithospheres away from modern spreading centers, as well as beneath young or rejuvenated continents with LAB depths ranging from around 60 to 125 km (Fig. 9). Interestingly, rare occurrences of alnoitic CO_2-rich intrusions with SiO_2 ~36 wt% have been reported at the surface of the ~120-km-thick lithosphere of the Ontong Java Plateau *(Neal and Davidson, 1989; Simonetti and Neal, 2010; Smart et al., 2019)*, and this SiO_2 content is well reproduced in our MAGLAB calculations at such LAB depth (i.e., ~35 wt% SiO_2; Figs 5B,

9). In addition, MAGLAB predicts mantle-derived melts with a SiO_2 content of ~40 wt% beneath ~90-km-thick lithosphere, similar to the petit-spot magmas erupted directly from the asthenospheric source located beneath the flexed sections of the oceanic lithosphere prior to entering subduction zones *(Hirano et al., 2006; Matsuno et al., 2010; Machida et al., 2017; Sato et al., 2018)*. Generation of kimberlites also fits well into this hypothesis, with primary melts with 15-35 wt% SiO_2 being produced at >120 to ~200 km depth beneath continental shields including cratons (Fig. 9; *Gudfinnsson and Presnall, 2005; Brey et al., 2009; Foley et al., 2009; Stamm and Schmidt, 2017; Tappe et al., 2017; Giuliani et al., 2019; Sun and Dasgupta, 2019*). Such carbonated silicate melt compositions can be equilibrated beneath typical LAB depths of undisturbed cratons (i.e., 180-250 km) in warmer thermal conditions, with T_P >~1350-1400°C, equivalent to the peripheries of modern mantle plumes or Early Proterozoic and Archean ambient upper mantle conditions (*Korenaga, 2008; Davies, 2009; Ganne and Feng, 2017; Aulbach and Arndt, 2019; Sun and Dasgupta, 2020*; see also Fig. 6B). However, many kimberlite occurrences at the Earth's surface were emplaced between 50-250 Ma *(Tappe et al., 2018)*, a period for which the Earth's mantle presented a thermal regime similar to present-day (difference in T_P <40-50°C; *Korenaga, 2008; Davies, 2009; Ganne and Feng, 2017; Aulbach and Arndt, 2019*). Furthermore, genetic connections between kimberlite magma generation and mantle plumes are still debated (see for example *Tappe et al., 2020*). Alternatively, primary transitional carbonated silicate melts can also be produced beneath such undisturbed cratons with higher H_2O content in the bulk peridotite (e.g., carbonatitic melts equilibrated near the LAB at 210 km depth in a mantle source with 140 wt ppm CO_2 – 240 wt ppm H_2O versus kimberlitic melts equilibrated in a mantle source with 140 wt ppm CO_2 – 720 wt ppm H_2O; see Section 4 and Fig. 8B), as is supported by the experimental work of *Stamm and Schmidt (2017)*. Therefore, our simulations indicate that presence of kimberlitic melts beneath undisturbed cratons may be related to greater H_2O enrichment in the mantle source. Similarly, either excess temperatures or H_2O enrichments in the mantle source would explain generation of basalts with >45 wt% SiO_2 beneath strongly disturbed cratons with drastically thinned lithospheres (~60-100 km) within our scenario (e.g., East African rift, Wyoming, North China; see *Aulbach, 2019*, and references therein).

The empirical observation that variations in lithosphere thickness primarily govern the compositional diversity of primitive mantle-derived magmatism *(Gudfinnsson and Presnall, 2005; Tappe et al., 2007)* is fully supported by MAGLAB modeling. The compositions of erupted magmas correspond to those equilibrated at LAB depths (Fig. 9), from where they appear to be extracted. This may explain why low-SiO_2 melts such as kimberlites and aillikites are mainly found under geologically reasonable conditions on continental shields including cratons, which are characterized by the deepest known lithosphere-asthenosphere boundaries at 150-250 km depths (e.g., *Aulbach et al., 2017; Tappe et al., 2018*) (Figs 7-9).

5.2. Testing of MAGLAB on the petrologically-geophysically constrained Society hotspot

Mantle geophysical anomalies such as high electrical conductivities and sharp seismic shear-wave velocity reductions have been reported at various locations worldwide, beneath oceanic and continental settings *(Evans et al., 2005; Baba et al., 2006, 2010, 2017a; Kawakatsu et al., 2009; Schmerr, 2012; Naif et al., 2013; Tada et al., 2016; Tharimena et al., 2017a,b; Rychert et al., 2019)*. The presence and role of volatile-bearing melts is indisputable in these regions *(Gaillard et al., 2008; Schmerr, 2012; Sifré et al., 2014; Tada et al., 2016; Katsura et al., 2017; Tharimena et al., 2017a,b; Rychert et al., 2019; Gardés et al., 2020)*. Among them, the Society hotspot in the Pacific Ocean is a good candidate to test MAGLAB since geochemical and geophysical boundary conditions in this ~70 Myr old oceanic lithosphere are rather well constrained *(Müller et al., 2008)*.

The Society hotspot originates from an ascending plume *(Adam et al., 2010)* which supplies more heat and higher volatile contents compared with the ambient convecting mantle *(Tada et al., 2016)*. The mantle potential temperature has been estimated within 1450-1500°C *(Herzberg and Asimow, 2008)*. The volatile content of the mantle source has been estimated at ~700 wt ppm CO_2 and 720 wt ppm H_2O by studying the degassing in submarine lavas from the Society hotspot *(Aubaud et al., 2005)*. Average major element compositions of near-primary OIBs erupted at various volcanic centers in the Society Islands have also been assessed, providing an estimation of the major element composition of melts produced from the plume beneath the Society hotspot *(Dasgupta et al., 2010)*. Besides, the Society hotspot presents an anomalously strong electrical signature, called "Zone A" *(Nolasco et al., 1998; Suetsugu et al., 2012; Tada et al., 2016)*. It extends from the lowest part of the upper mantle to approximately 50 km below sea level. Electrical conductivities above 10^{-1} S m^{-1} are recorded below ~90 km depth, with a maximum of $10^{-0.3}$ S m^{-1} at about 130-150 km (Fig. 10, and see profile "Anomaly Zone A" in Fig. 11; *Tada et al., 2016*). This signature is clearly distinct from the electrical conductivity of neighbouring mantle, being about 1 to 2 log units lower (see profile "TIARES" in Fig. 11; *Tada et al., 2016*).

We performed MAGLAB simulations using the pressures, temperatures and volatile contents reported for the Society hotspot as inputs, corresponding to the G13R1450 thermal model with T_P = 1450°C from *Grose and Afonso (2013)*, together with ~700 wt ppm CO_2 and 720 wt ppm H_2O. Around the LAB beneath this ~70 Myr old oceanic lithosphere, at approximately 120±10 km depth, MAGLAB yields ~1.2 to 1.5 wt% of primary silicate-rich melt, bearing about 3.5-3.8 wt% H_2O and 4.7-5.6 wt% CO_2. The SiO_2 content is within the range 39.2-40.4 wt%, i.e. 43.1-44.1 wt% on a volatile-free basis, compatible with the 43-48 wt% estimations of near-primary average SiO_2 contents of OIBs reported for the Society islands by *Dasgupta et al. (2010)* (Fig. 10). Good agreement is also observed for other major elements, such as Al_2O_3, FeO, MgO, CaO and alkalis (Fig. 10).

Simulated electrical conductivities are also in very good agreement (Fig. 10), being $10^{-0.59}$-$10^{-0.48}$ S m^{-1} compared to the $10^{-0.50}$-$10^{-0.29}$ S m^{-1} measured between 110 and 130 km depth *(Tada et al., 2016)*. Hence, this case study demonstrates the robustness of MAGLAB in reproducing both petrological and geophysical data in a partially molten mantle column/volume. The presence of 1.2-1.5 wt% of volatile-bearing silicate melts beneath the Society hotspot as inferred by MAGLAB raises the question about mobility relative to host mantle rocks. According to *Gaillard et al. (2019)*, such melts should percolate at 10-14 cm yr^{-1}, whereas mantle plume ascent is estimated at ~20-40 cm yr^{-1} on the basis of geodynamic

simulations *(Arnould et al., 2020)*. Melt ascent via convection thus appears to dominate over melt percolation in this oceanic mantle 'hotspot' setting.

5.3. Heterogeneous distribution of volatile-bearing melts in the oceanic upper mantle

Figure 11 reports electrical conductivity profiles derived from magnetotelluric surveys on various locations in the Pacific and Atlantic, from very young (<5 Ma) to relatively old (130 Ma) seafloors. These profiles illustrate the heterogeneous electrical signature of the oceanic upper mantle, spanning the range of 10^{-3}-$10^{-0.3}$ S m^{-1}, and which must then be connected to the heterogeneities in temperature or volatile content in Earth's upper mantle. Figure 11 also reports the range of electrical conductivities for partially molten mantle peridotite calculated by MAGLAB from: (i) old and cold mantle (130 Ma geotherm of G13R1300 model with T_P = 1300°C from *Grose and Afonso (2013)*) that is highly depleted in volatiles (20 wt ppm CO_2 and 50 wt ppm H_2O; *Dasgupta and Hirschmann, 2010; Shimizu et al., 2019*) to (ii) young and hot mantle (0 Ma geotherm of G13R1450 model with T_P = 1450°C from *Grose and Afonso (2013)*) that is highly enriched in volatiles (700 wt ppm CO_2 and 720 wt ppm H_2O; *Aubaud et al., 2005*).

MAGLAB simulations cover the range of mantle conductivities observed beneath the seafloors of various ages well. The high electrical conductivities of >10^{-1} S m^{-1} reported at mantle depths of <130 km beneath the outer rise of Cocos plate seafloor (see profile "SERPENT" in Fig. 11; *Naif et al., 2013; Naif, 2013*), the Reykjanes Ridge (see profile "RAMESSES AVR Centre" in Fig. 11; *Heinson et al., 2000*), or the Society hotspot (see profile "Anomaly Zone A" in Fig. 11; *Tada et al., 2014*) require melt fractions of up to 0.5-1 wt% resulting from a high degree of volatile enrichment, even when elevated T_P are accounted for (see Sections 4 and 5.2). Very high mantle electrical conductivities >$10^{-0.5}$ S m^{-1}, e.g. beneath the ultraslow-spreading Mohns Ridge, would require even higher melt fractions of >>1 wt% *(Johansen et al., 2019)*. On the other hand, the lowest electrical conductivities with values of ≤10^{-2} S m^{-1} are compatible with the presence of very low melt fractions, i.e. <<0.1 wt%, in depleted mantle regions. Within the asthenosphere, at >125 km depth, mantle conductivities are typically between 10^{-2} and 10^{-1} S m^{-1} implying melt fractions of <1 wt% in all cases (Fig. 11).

Combined petrological and electrical simulations using MAGLAB confirm that the high variability of conductivity profiles in the oceanic upper mantle is related to strong heterogeneities in its volatile content *(Herzberg and Asimow, 2008; Hirschmann, 2010, 2018; Ganne and Feng, 2017; La Voyer et al., 2017; Clerc et al., 2018)*. Highly variable amounts of interconnected volatile-bearing melts, generally <<1 wt%, may be widespread in the uppermost convecting mantle, but their 'geophysical' detection is challenging if very small fractions are produced *(Gaillard et al., 2019; Gardés et al., 2020)*. This could explain the rarity of a geophysically detected discontinuity near cratonic LABs *(Eaton et al., 2009; Mancinelli et al., 2017)*. Alternatively, this reflects that the mantle at 200-250 km is too reducing to stabilize carbonated melt *(Aulbach, 2019)*. MAGLAB then allows providing bounds on the volatile content for such contexts. Moreover, heterogeneities in mantle volatile content question the role of melt migration in redistributing volatiles. For instance, the very high electrical conductivities reported in the relatively ambient upper mantle beneath Mohns Ridge might be caused by large melt fractions of >>1 wt%, originated from melt migration and accumulation processes *(Johansen et al., 2019)*, and shaping high bulk volatile contents (>>500 wt ppm CO_2-H_2O). Volatile and, thus, melt migration plus redistribution can be simulated if dynamic processes including mantle convection are combined with a rigorous petrological framework for mantle melting as provided here by MAGLAB (see also *Keller et al., 2016, 2017; Clerc et al., 2018*). However, further development of these multi-disciplinary modeling techniques is required to continue the quest for better understanding mantle melting processes and their implications for crust-mantle evolution.

6. Conclusion

MAGLAB is a new computing platform that models melt compositions, melt fractions and electrical conductivity at pressure-temperature conditions and volatile contents relevant to the upper mantle (i.e., 2-10 GPa, 900-1700°C, depleted to enriched peridotite compositions, up to many thousands of wt ppm of CO_2 and H_2O). The platform can be accessed free of charge online at *http://calcul-isto.cnrs-orleans.fr/apps/maglab/*. MAGLAB can be used to model melting processes in oceanic and continental intraplate settings, including kimberlite melt formation beneath cratons. Our modeling results show that erupted intraplate magma compositions correspond to the melts equilibrated near LAB depths, and that a diversity of magma types can be produced from a homogeneous peridotitic mantle source. For 'normal' upper mantle with 1350°C potential temperature and average volatile content of 140 wt ppm CO_2 and 240 wt ppm H_2O, carbonatitic melt compositions with <15 wt% SiO_2 are produced beneath 200-250 km thick cratonic lithospheres and basanitic-basaltic melt compositions with >40 wt% SiO_2 beneath mature ocean basins with much thinner lithospheres (i.e., 60-100 km thick). Melts with SiO_2 contents between 15-35 wt% such as kimberlites form only at high pressures corresponding to depths of ≥120 km. Their formation is enhanced in peridotitic mantle sources with high H_2O contents in addition to CO_2. In a test case, our combined petrological and geophysical modeling reproduces known compositions of erupted melts and the measured mantle electrical conductivity for the Society hotspot. An important finding from MAGLAB simulations is that the commonly observed variability of mantle electrical conductivity can be linked to the presence and heterogeneous distribution of small volumes (generally <<1 wt%) of volatile-bearing melts within Earth's upper mantle.

Acknowledgements

We thank Mark Jellinek for manuscript handling, as well as Michel Grégoire and two anonymous reviewers for their valuable comments. We also sincerely thank Tim Holland and Eleanor Green for helpful discussions whose our modeling work has benefited, and Claude Herzberg for providing comments on a previous version of the manuscript. This work was part of the ElectroLith project and benefited from funding by the European Research Council (ERC project #279790) and the French agency for research (ANR project #2010 BLAN62101). GR also gratefully acknowledges funding by the French agency for research under grant Labex VOLTAIRE ANR-10-LABX-100-01. The DEEP Research Group at the University of Johannesburg is supported by the DSI-NRF CIMERA Center of Excellence, South Africa. MM was partially funded through a scholarship from the Department of Science and Technology Research Chairs Initiative as administered by the NRF South Africa (SARChI Chair grant #64779 awarded to K.S. Viljoen), which we gratefully acknowledge. Additional financial support was provided to ST via the NRF-IPRR funding framework. MM also gratefully acknowledges funding from the European Union's Horizon 2020 research and innovation program under the Marie Skłodowska-Curie grant agreement No. 842339. SA gratefully acknowledges funding by the German Research Foundation under grant AU356/11. Readers can access data and additional information not reported in the main paper via the supporting online resources.

Appendix A. Supplementary Information

References

Adam, C., Yoshida, M., Isse, T., Suetsugu, D., Fukao, Y., & Barruol, G. (2010). South Pacific hotspot swells dynamically supported by mantle flows. *Geophysical Research Letters*, *37*, 6 pp., doi: 10.1029/2010GL042534.

An, M., Wiens, D.A., Zhao, Y., Feng, M., Nyblade, A., Kanao, M., Li, Y., Maggi, A., Lévêque, J.-J. (2015). Temperature, lithosphere-asthenosphere boundary, and heat flux beneath the Antarctic Plate inferred from seismic velocities. *Journal of Geophysical Research*, *120*, 8720-8742, doi: 10.1002/2014JB011332.

Ariskin, A.A. (1999). Phase equilibria modeling in igneous petrology: use of COMAGMAT model for simulating fractionation of ferro-basaltic magmas and the genesis of high-alumina basalt. *Journal of Volcanology and Geothermal Research*, *90*, 115-162, doi: 10.1016/S0377-0273(99)00022-0.

Arnould, M., Coltice, N., Flament, N., & Mallard, C. (2020). Plate tectonics and mantle controls on plume dynamics. *Earth and Planetary Science Letters*, *547*, 15 pp., doi: 10.1016/j.epsl.2020.116439.

Aubaud, C., Pineau, F., Hékinian, R., & Javoy, M. (2005). Degassing of CO_2 and H_2O in submarine lavas from the Society hotspot. *Earth and Planetary Science Letters*, *235*, 511-527, doi: 10.1016/j.epsl.2005.04.047.

Aulbach, S. (2019). Cratonic Lithospheric Discontinuities: Dynamics of Small-Volume Melting, Metacratonization, and a Possible Role for Brines: Chapter 10 in *Lithospheric Discontinuities*. Edited by Huaiyu Yuan and Barbara Romanowicz, doi: 10.1002/9781119249740.ch10.

Aulbach, S., & Arndt, N. T. (2019) Eclogites as Palaeodynamic Archives: Evidence for Warm (not hot) and Depleted (but heterogeneous and evolving) Archaean Ambient Mantle. *Earth and Planetary Science Letters*, *505*, 162-172, doi: 10.1016/j.epsl.2018.10.025.

Aulbach, S., Massuyeau, M., & Gaillard, F. (2017). Origins of cratonic mantle discontinuities: A view from petrology, geochemistry and thermodynamic models. *Lithos*, *268–271*, 364–382, doi: 10.1016/j.lithos.2016.11.004.

Baba, K., Chave, A.D., Evans, R.L., Hirth, G., & Mackie, R.L. (2006). Mantle dynamics beneath the East Pacific Rise at 17°S: Insights from the Mantle Electromagnetic and Tomography (MELT) experiment. *Journal of Geophysical Research*, *111*, 18 pp., doi: 10.1029/2004JB003598.

Baba, K., Chen, J., Sommer, M., Utada, H., Geissler, W.H., Jokat, W., & Jegen, M. (2017a). Marine magnetotellurics imaged no distinct plume beneath the Tristan da Cunha hotspot in the southern Atlantic Ocean. *Tectonophysics*, *716*, 52-63, doi: 10.1016/j.tecto.2016.09.033.

Baba, K., Tada, N., Matsuno, T., Liang, P., Li, R., Zhang, L., Shimizu, H., Abe, N., Hirano, N., Ichiki, M., & Utada, H. (2017b). Electrical conductivity of old oceanic mantle in the northwestern Pacific I: 1-D profiles suggesting differences in thermal structure not predictable from a plate cooling model. *Earth, Planets and Space*, *69*, 23 pp., doi: 10.1186/s40623-017-0697-0.

Baba, K., Tada, N., Zhang, L., Liang, P., Shimizu, H., & Utada, H. (2013). Is the electrical conductivity of the northwestern Pacific upper mantle normal? *Geochemistry, Geophysics, Geosystems*, *14*, 4969-4979, doi: 10.1002/2013GC004997.

Baba, K., Utada, H., Goto, T.-N., Kasaya, T., Shimizu, H., & Tada, N. (2010). Electrical conductivity imaging of the Philippine Sea upper mantle using seafloor magnetotelluric data. *Physics of the Earth and Planetary Interiors*, *183*, 44-62, doi: 10.1016/j.pepi.2010.09.010.

Ballmer, M.D., Ito, G., van Hunen, J., & Tackley, P.J. (2011). Spatial and temporal variability in Hawaiian hotspot volcanism induced by small-scale convection. *Nature Geoscience*, *4*, 457-460, doi: 10.1038/NGEO1187.

Baudouin, C., & Parat, F. (2020). Phlogopite-Olivine Nephelinites Erupted During Early Stage Rifting, North Tanzanian Divergence. *Frontiers in Earth Science*, *8*, 22 pp., doi: *10.3389/feart.2020.00277*.

Baudouin, C., Parat, F., Denis, C.M.M., & Mangasini, F. (2016). *Contributions to Mineralogy and Petrology*, *171*, 20 pp., doi: 10.1007/s00410-016-1273-5.

Becker, M., & le Roex, A.P. (2006). Geochemistry of South African On- and Off-craton, Group I and Group II Kimberlites: Petrogenesis and Source Region Evolution. *Journal of Petrology*, *47*, 673-703, doi: 10.1093/petrology/egi089.

Bodinier, J.-L., Vasseur, G., Vernieres, J., Dupuy, C., & Fabries, J. (1990). Mechanisms of Mantle Metasomatism: Geochemical Evidence from the Lherz Orogenic Peridotite. *Journal of Petrology*, *31*, 597-628, doi: 10.1093/petrology/31.3.597.

Brey, G.P., Bulatov, V.K., & Girnis, A.V. (2009). Influence of water and fluorine on melting of carbonated peridotite at 6 and 10 GPa. *Lithos*, *112S*, 249-259, doi: 10.1016/j.lithos.2009.04.037.

Carmichael, I.S.E., Nicholls, J., Smith, A.L. (1970). Silica activity in igneous rocks. *American Mineralogist*, *55*, 246–263, doi: 10.1007/BF00373791.

Chantel, J., Manthilake, G., Andrault, D., Novella, D., Yu, T., & Wang, Y. (2016). Experimental evidence supports mantle partial melting in the asthenosphere. *Science Advances*, *2*, e1600246, doi: 10.1126/sciadv.1600246.

Clerc, F., Behn, M.D., Parmentier, E.M., & Hirth, G. (2018). Predicting Rates and Distribution of Carbonate Melting in Oceanic Upper Mantle: Implications for Seismic Structure and Global Carbon Cycling. Geophysical Research Letters, 45, 6944-6953, doi: 10.1029/2018GL078142.

Connolly, J.A.D. (2005). Computation of phase equilibria by linear programming: A tool for geodynamic modeling and its application to subduction zone decarbonation. *Earth and Planetary Science Letters*, *236*, 524-541, doi: 10.1016/j.epsl.2005.04.033.

Dasgupta, R. (2018). Volatile-bearing partial melts beneath oceans and continents-where, how much, and of what compositions? *American Journal of Science*, *318*, 141-165, doi: 1 0.2475/01.2018.06.

Dasgupta, R., & Hirschmann, M.M. (2006). Melting in the Earth's deep upper mantle caused by carbon dioxide. *Nature*, *440*, 659-662, doi: 10.1038/nature04612.

Dasgupta, R., & Hirschmann, M.M. (2010). The deep carbon cycle and melting in Earth's interior. *Earth and Planetary Science Letters*, *298*, 1-13, doi: 10.1016/j.epsl.2010.06.039.

Dasgupta, R., Jackson, M.G., & Lee, C.-T. A. (2010). Major element chemistry of ocean island basalts — Conditions of mantle melting and heterogeneity of mantle source. *Earth and Planetary Science Letters*, *289*, 377-392, doi: 10.1016/j.epsl.2009.11.027.

Dasgupta, R., Hirschmann, M.M., & Smith, N.D. (2007). Water follows carbon: CO_2 incites deep silicate melting and dehydration beneath mid-ocean ridges. *Geology, 35*, 135-138, doi: 10.1130/G22856A.1.

Dasgupta, R., Mallik, A., Tsuno, K., Withers, A.C., Hirth, G., & Hirschmann, M.M. (2013). Carbon-dioxide-rich silicate melt in the Earth's upper mantle. *Nature, 493*, 211-215, doi: 10.1038/nature11731.

Davies, G.F. (2009). Effect of plate bending on the Urey ratio and the thermal evolution of the mantle. *Earth and Planetary Science Letters, 287*, 513-518, doi: 10.1016/j.epsl.2009.08.038.

Davies, D.R., Rawlinson, N., Iaffaldano, G., & Campbell, I.H. (2015). Lithospheric controls on magma composition along Earth's longest continental hotspot track. *Nature, 525*, 511-514, doi: 10.1038/nature14903.

DeCapitani, C., & Kirschen, M. (1998). A generalized multicomponent excess function with application to immiscible liquids in the system CaO SiO2-TiO2. *Geochimica et Cosmochimica Acta, 62*, 3753-3763, doi: 10.1016/S0016-7037(98)00319-6.

Doucelance, R., Hammouda, T., Moreira, M., & Martins, J.C. (2010). Geochemical constraints on depth of origin of oceanic carbonatites: The Cape Verde case. *Geochimica et Cosmochimica Acta, 74*, 7261–7282, doi: 10.1016/j.gca.2010.09.024.

Eaton, D.W., Darbyshire, F., Evans, R.L., Grütter, H., Jones, A.G., & Yuan, X. (2009). The elusive lithosphere–asthenosphere boundary (LAB) beneath cratons. *Lithos, 109*, 1-22, doi: 10.1016/j.lithos.2008.05.009.

Eggler, D.H., 1976. Does CO_2 cause partial melting in the low-velocity layer of the mantle? Geology, 4, 69–72, doi: https://doi.org/10.1130/0091-7613(1976)4<69:DCCPMI>2.0.CO;2.

Eguchi, J., & Dasgupta, R. (2018). Redox state of the convective mantle from CO_2-trace element systematics of oceanic basalts. *Geochemical Perspectives Letters, 8*, 17-21, doi: 10.7185/geochemlet.1823.

Ellam, R.M. (1992). Lithospheric thickness as a control on basalt geochemistry. *Geology, 20*, 153-156, doi: 10.1130/0091-7613(1992)020<0153:LTAACO>2.3.CO;2.

Evans, R.L., Hirth, G., Baba, K., Forsyth, D., Chave, A., & Mackie, R. (2005). Geophysical evidence from the MELT area for compositional controls on oceanic plates. *Nature, 437*, 249-252, doi: 10.1038/nature04014.

Fischer, K.M., Ford, H.A., Abt, D.L., & Rychert, C.A. (2010). The Lithosphere-Asthenosphere Boundary. *Annual Review of Earth and Planetary Sciences, 38*, 551-575, doi: 10.1146/annurev-earth-040809-152438.

Foley, S.F. (2008). Rejuvenation and erosion of the cratonic lithosphere. *Nature Geoscience, 1*, 503-510, doi: 10.1038/ngeo261.

Foley, S.F., Yaxley, G.M., Rosenthal, A., Buhre, S., Kiseeva, E.S., Rapp, R.P., & Jacob, D.E. (2009). The composition of near-solidus melts of peridotite in the presence of CO_2 and H_2O between 40 and 60 kbar. *Lithos, 112S*, 274-283, doi: 10.1016/j.lithos.2009.03.020.

French, S.W., & Romanowicz, B. (2015). Broad plumes rooted at the base of the Earth's mantle beneath major hotspots. *Nature, 525*, 95-99, doi: 10.1038/nature14876.

Gaillard, F., Malki, M., Iacono-Marziano, G., Pichavant, M., & Scaillet, B. (2008). Carbonatite Melts and Electrical Conductivity in the Asthenosphere. *Science*, *322*, 1363-1365, 1126/science.1164446.

Gaillard, F., Scaillet, B., Pichavant, M., & Iacono-Marziano, G. (2015). The redox geodynamics linking basalts and their mantle sources through space and time. *Chemical Geology*, *418*, 217-233, doi: 10.1016/j.chemgeo.2015.07.030.

Gaillard, F., Sator, N., Gardés, E., Guillot, B., Massuyeau, M., Sifré, D., Hammouda, T., & Richard, G. (2019). The Link between the Physical and Chemical Properties of Carbon-Bearing Melts and Their Application for Geophysical Imaging of Earth's Mantle. In B. Orcutt, I. Daniel, & R. Dasgupta (Eds.), *Deep Carbon: Past to Present* (pp. 163-187). *Cambridge: Cambridge University Press*.

Ganne, J., & Feng, X. (2017). Primary magmas and mantle temperatures through time. *Geochemistry, Geophysics, Geosystems*, *18*, 872-888, doi: 10.1029/2019GC008227.

Gardés, E., Gaillard, F., & Tarits, P. (2014). Toward a unified hydrous olivine electrical conductivity law. *Geochemistry, Geophysics, Geosystems*, *15*, 4984-5000, doi: 10.1002/2014GC005496.

Gardés, E., Laumonier, M., Massuyeau, M., & Gaillard, F. (2020). Unravelling partial melt distribution in the oceanic low velocity zone. *Earth and Planetary Science Letters*, *540*, 116242, doi: 10.1016/j.epsl.2020.116242.

Ghiorso, M.S., & Sack, R.O. (1995). Chemical mass transfer in magmatic processes IV. A revised and internally consistent thermodynamic model for the interpolation and extrapolation of liquid-solid equilibria in magmatic systems at elevated temperatures and pressures. *Contributions to Mineralogy and Petrology*, *119*, 197-212, doi: 10.1007/BF00307281.

Ghiorso, M.S., Hirschmann, M.M., Reiners, P.W., & Kress, V.C. (2002). The pMELTS: A revision of MELTS for improved calculation of phase relations and major element partitioning related to partial melting of the mantle to 3 GPa. *Geochemistry, Geophysics, Geosystems*, *3*, 36 pp., doi: 10.1029/2001GC000217.

Ghiorso, M.S., & Gualda, G.A.R. (2015). An H_2O–CO_2 mixed fluid saturation model compatible with rhyolite-MELTS. *Contributions to Mineralogy and Petrology*, *169*, doi:10.1007/s00410-015-1141-8.

Ghosh, S., Litasov, K., & Ohtani, E. (2014). Phase relations and melting of carbonated peridotite between 10 and 20 GPa: a proxy for alkali- and CO_2-rich silicate melts in the deep mantle. Contributions to Mineralogy and Petrology, 167, 23 pp., doi: 10.1007/s00410-014-0964-z.

Giuliani, A., & Pearson, D.G. (2019). Kimberlites: From Deep Earth to Diamond Mines. *Elements*, *15*, 377-380, doi: 10.2138/gselements.15.6.377.

Grégoire, M., Bell, D.R., & le Roex, A.P. (2003). Garnet Lherzolites from the Kaapvaal Craton (South Africa): Trace Element Evidence for a Metasomatic History. *Journal of Petrology*, *44*, 629-657, doi: 10.1093/petrology/44.4.629.

Grose, C.J., & Afonso, J.-C. (2013). Comprehensive plate models for the thermal evolution of oceanic lithosphere. *Geochemistry, Geophysics, Geosystems*, *14*, 3751-3778, doi: 10.1002/ggge.20232.

Grose, C.J., & Afonso, J.-C. (2019). Chemical Disequilibria, Lithospheric Thickness, and the Source of Ocean Island Basalts. *Journal of Petrology*, *60*, 755-790, doi: 10.1093/petrology/egz012.

Gualda, G.A.R., Ghiorso, M.S., Lemons, R.V., & Carley, T.L. (2012). Rhyolite-MELTS: a Modified Calibration of MELTS Optimized for Silica-rich, Fluid-bearing Magmatic Systems. *Journal of Petrology*, *53*, 875-890, doi: 10.1093/petrology/egr080.

Gudfinnsson, G.H., & Presnall, D.C. (2005). Continuous Gradations among Primary Carbonatitic, Kimberlitic, Melilititic, Basaltic, Picritic, and Komatiitic Melts in Equilibrium with Garnet Lherzolite at 3–8 GPa. *Journal of Petrology*, *46*, 1645-1659, doi: 10.1093/petrology/egi029.

Guo, P., Niu, Y., Sun, P., Gong, H., & Wang, X. (2020). Lithosphere thickness controls continental basalt compositions: An illustration using Cenozoic basalts from eastern China. *Geology*, *48*, 128-133, doi: 10.1130/G46710.1.

Haase, K.M. (1996). The relationship between the age of the lithosphere and the composition of oceanic magmas: Constraints on partial melting, mantle sources and the thermal structure of the plates. *Earth and Planetary Science Letters*, *144*, 75-92, doi: 10.1016/0012-821X(96)00145-8.

Hammouda, T., & Keshav, S. (2015). Melting in the mantle in the presence of carbon: Review of experiments and discussion on the origin of carbonatites. *Chemical Geology*, *418*, 171-188, doi: 10.1016/j.chemgeo.2015.05.018.

Hauri, E., Cottrell, E., Kelley, K., Tucker, J., Shimizu, K., Voyer, M., Marske, J., & Saal, A. (2019). Carbon in the Convecting Mantle. In B. Orcutt, I. Daniel, & R. Dasgupta (Eds.), *Deep Carbon: Past to Present* (pp. 237-275). *Cambridge: Cambridge University Press*.

Heinson, G., Constable, S., & White, A. (2000). Episodic Melt Transport at Mid-Ocean Ridges Inferred from Magnetotelluric Sounding. *Geophysical Research Letters*, *27*, 2317-2320, doi: 10.1029/2000GL011473.

Herzberg, C., & Asimow, P.D. (2008). Petrology of some oceanic island basalts: PRIMELT2.XLS software for primary magma calculation. *Geochemistry, Geophysics, Geosystems*, *9*, 25 pp., doi: 10.1029/2008GC002057.

Hirano, N., Takahashi, E., Yamamoto, J., Abe, N., Ingle, S.P., Kaneoka, I., Hirata, T., Kimura, J.-I., Ishii, T., Ogawa, Y., Machida, S., & Suyehiro, K. (2006). Volcanism in Response to Plate Flexure. *Science*, *313*, 1426-1428, doi: 10.1126/science.1128235.

Hirschmann, M.M. (2000). Mantle solidus: Experimental constraints and the effects of peridotite composition. *Geochemistry, Geophysics, Geosystems*, *1*, 26 pp., doi: 10.1029/2000GC000070.

Hirschmann, M.M. (2010). Partial melt in the oceanic low velocity zone. *Physics of the Earth and Planetary Interiors*, *179*, 60-71, doi: 10.1016/j.pepi.2009.12.003.

Hirschmann, M.M. (2018). Comparative deep Earth volatile cycles: The case for C recycling from exosphere/mantle fractionation of major (H_2O, C, N) volatiles and from H_2O/Ce, CO_2/Ba, and CO_2/Nb exosphere ratios. *Earth and Planetary Science Letters*, *502*, 262-273, doi: 10.1016/j.epsl.2018.08.023.

Hirschmann, M.M., Kogiso, T., Baker, M.B., & Stolper, E.M. (2003). Alkalic magmas generated by partial melting of garnet pyroxenite. *Geology*, *31*, 481-484, doi: 10.1130/0091-7613(2003)031<0481:AMGBPM>2.0.CO;2.

Hirschmann, M.M., Tenner, T., Aubaud, C., & Withers, A.C. (2009). Dehydration melting of nominally anhydrous mantle: The primacy of partitioning. *Physics of the Earth and Planetary Interiors*, *176*, 54-68, doi: 10.1016/j.pepi.2009.04.001.

Holland, T.J.B., & Powell, R. (2011). An improved and extended internally consistent thermodynamic dataset for phases of petrological interest, involving a new equation of state for solids. *Journal of Metamorphic Geology*, *29*, 333-383, doi: 10.1111/j.1525-1314.2010.00923.x.

Holtzmann, B. (2016). Questions on the existence, persistence and mechanical effects of a very small melt fraction in the asthenosphere. *Geochemistry, Geophysics, Geosystems*, *17*, 470– 484, doi:10.1002/2015GC006102.

Humphreys, E.R., & Niu, Y. (2009). On the composition of ocean island basalts (OIB): The effects of lithospheric thickness variation and mantle metasomatism. *Lithos*, *112*, 118-136, doi: 10.1016/j.lithos.2009.04.038.

Jaupart, C, & Mareschal, J.C. (1999). The thermal structure and thickness of continental roots. *Lithos*, *48*, 93-114, doi: 10.1016/S0024-4937(99)00023-7.

Johansen, S.E., Panzner, M., Mittet, R., Amundsen, H.E.F., Lim, A., Vik, E., Landrø, M., & Arntsen, B. (2019). Deep electrical imaging of the ultraslow-spreading Mohns Ridge. *Nature*, *567*, 379-383, doi: 10.1038/s41586-019-1010-0.

Katsura, T., Baba, K., Yoshino, T., & Kogiso, T. (2017). Electrical conductivity of the oceanic asthenosphere and its interpretation based on laboratory measurements. *Tectonophysics*, *717*, 162-181, doi: 10.1016/j.tecto.2017.07.001.

Kawakatsu, H., & Utada, H. (2017). Seismic and Electrical Signatures of the Lithosphere–Asthenosphere System of the Normal Oceanic Mantle. *Annual Review of Earth and Planetary Sciences*, *45*, 139-167, doi: 10.1146/annurev-earth-063016-020319.

Kawakatsu, H., Kumar, P., Takei, Y., Shinohara, M., Kanazawa, T., Araki, E., & Suyehiro, K. (2009). Seismic Evidence for Sharp Lithosphere-Asthenosphere Boundaries of Oceanic Plates. *Science*, *324*, 499-502, doi: 10.1126/science.1169499.

Key, K., Constable, S., Liu, L., & Pommier, A. (2013). Electrical image of passive mantle upwelling beneath the northern East Pacific Rise. *Nature*, *495*, 499-502, doi: 10.1038/nature11932.

Keller, T., & Katz, R.F. (2016). The Role of Volatiles in Reactive Melt Transport in the Asthenosphere. *Journal of Petrology*, *57*, 1073-1108, doi: 10.1093/petrology/egw030.

Keller, T., Katz, R.F., & Hirschmann, M.M. (2017). Volatiles beneath mid-ocean ridges: Deep melting, channelised transport, focusing, and metasomatism. *Earth and Planetary Science Letters*, *464*, 55-68, doi: 10.1016/j.epsl.2017.02.006.

Klein-BenDavid, O., Izraeli, E.S., Hauri, E., & Navon, O. (2007). Fluid inclusions in diamonds from the Diavik mine, Canada and the evolution of diamond-forming fluids. *Geochimica et Cosmochimica Acta*, *71*, 723-744, doi: 10.1016/j.gca.2006.10.008.

Korenaga, J. (2008). Urey ratio and the structure and evolution of Earth's mantle. *Reviews of Geophysics*, *46*, 32 pp., doi: 10.1029/2007RG000241.

le Roex, A.P. (1986). Geochemical correlation between southern African kimberlites and South Atlantic hotspots. Nature, 324, 243-245, doi: 10.1038/324243a0.

Lee, C.-T. A. (2003). Compositional variation of density and seismic velocities in natural peridotites at STP conditions: Implications for seismic imaging of compositional

heterogeneities in the upper mantle. *Journal of Geophysical Research*, *108*, 20 pp., doi: 10.1029/2003JB002413.

Le Voyer, M., Kelley, K.A., Cottrell, E., Hauri, E.H. (2017). Heterogeneity in mantle carbon content from CO_2-undersaturated basalts. Nature Communications, 8, 8 pp., doi: 10.1038/ncomms14062.

Liu, J., Cai, R., Pearson, G., & Scott, J.M. (2019). Thinning and destruction of the lithospheric mantle root beneath the North China Craton: A review. Earth-Science Reviews, 196, 18 pp., doi: 10.1016/j.earscirev.2019.05.017.

Lizarralde, D., Chave, A., Hirth, G., & Schultz, A. (1995). Northeastern Pacific mantle conductivity profile from long-period magnetotelluric sounding using Hawaii-to-California submarine cable data. *Journal of Geophysical Research*, *100*, 17837-17854, doi: 10.1029/95JB01244.

Lu, J., Tilhac, R., Griffin, W.L., Zheng, J., Xiong, Q., Oliveira, B., & O'Reilly, S.Y. (2020). Lithospheric memory of subduction in mantle pyroxenite xenoliths from rift-related basalts. *Earth and Planetary Science Letters*, *544*, 14 pp., doi: 10.1016/j.epsl.2020.116365.

Machida, S., Kogiso, T., & Hirano, N. (2017). Petit-spot as definitive evidence for partial melting in the asthenosphere caused by CO_2. *Nature Communications*, *8*, 7 pp., doi: 10.1038/ncomms14302.

Mancinelli, N.J., Fischer, K.M., & Dalton, C.A. (2017). How Sharp Is the Cratonic Lithosphere-Asthenosphere Transition? *Geophysical Research Letters*, *44*, 10189-10197, doi: 10.1002/2017GL074518.

Marty, B. (2012). The origins and concentrations of water, carbon, nitrogen and noble gases on Earth. *Earth and Planetary Science Letters*, *313-314*, 56-66, doi: 10.1016/j.epsl.2011.10.040.

Massuyeau, M., Gardés, E., Morizet, Y., & Gaillard, F. (2015). A model for the activity of silica along the carbonatite–kimberlite–melilitite–basanite melt compositional joint. *Chemical Geology*, *418*, 206-216, doi: 10.1016/j.chemgeo.2015.07.025.

Mather, K.A., Pearson, D.G., McKenzie, D., Kjarsgaard, B.A., & Priestley, K. (2011). Constraints on the depth and thermal history of cratonic lithosphere from peridotite xenoliths, xenocrysts and seismology. *Lithos*, *125*, 729-742, doi: 10.1016/j.lithos.2011.04.003.

Matsuno, T., Seama, N., Evans, R.L., Chave, A.D., Baba, K., White, A., Goto, T.-N., Heinson, G., Boren, G., Yoneda, A., & Utada, H. (2010). Upper mantle electrical resistivity structure beneath the central Mariana subduction system. *Geochemistry, Geophysics, Geosystems*, *11*, 24 pp., doi: 10.1029/2010GC003101.

McKenzie, D., & Bickle, M.J. (1988). The Volume and Composition of Melt Generated by Extension of the Lithosphere. *Journal of Petrology*, *29*, 625-679, doi: 10.1093/petrology/29.3.625.

McKenzie, D., Jackson, J., & Priestley, K. (2005). Thermal structure of oceanic and continental lithosphere. *Earth and Planetary Science Letters*, *233*, 337-349, doi: 10.1016/j.epsl.2005.02.005.

Moussallam, Y., Longpré, M.-A., McCammon, C., Gomez-Ulla, A., Rose-Koga, E.F., Scaillet, B., Peters, N., Gennaro, E., Paris, R., & Oppenheimer, C. (2019). Mantle plumes are oxidised. *Earth and Planetary Science Letters*, 527, 10 pp., doi: 10.1016/j.epsl.2019.115798.

Moussallam, Y., Morizet, Y., & Gaillard, F. (2016). H_2O–CO_2 solubility in low SiO_2-melts and the unique mode of kimberlite degassing and emplacement. *Earth and Planetary Science Letters*, *447*, 151-160, doi: 10.1016/j.epsl.2016.04.037.

Müller, R.D., Sdrolias, M., Gaina, C., & Roest, W.R. (2008). Age, spreading rates, and spreading asymmetry of the world's ocean crust. *Geochemistry, Geophysics, Geosystems*, *9*, 19 pp., doi: 10.1029/2007GC001743.

Naif, S. (2018). An upper bound on the electrical conductivity of hydrated oceanic mantle at the onset of dehydration melting. *Earth and Planetary Science Letters*, *482*, 357-366, doi: 10.1016/j.epsl.2017.11.024.

Naif, S., Key, K., Constable, S., & Evans R.L. (2013). Melt-rich channel observed at the lithosphere–asthenosphere boundary. *Nature*, *495*, 356-359, doi: 10.1038/nature11939.

Neal, C.R., & Davidson, J.P. (1989). An unmetasomatized source for the Malaitan alnöite (Solomon Islands): petrogenesis involving zone refining, megacryst fractionation, and assimilation of oceanic lithosphere. *Geochimica et Cosmochimica Acta*, *53*, 1975-1990, doi: 10.1016/0016-7037(89)90318-9.

Ni, H., Keppler, H. & Behrens, H. (2011). Electrical conductivity of hydrous basaltic melts: implications for partial melting in the upper mantle. *Contributions to Mineralogy and Petrology*, *162*, 637–650, doi: 10.1007/s00410-011-0617-4.

Niu, Y., & Green, D.H. (2018). The petrological control on the lithosphere-asthenosphere boundary (LAB) beneath ocean basins. *Earth-Science Reviews*, *185*, 301-307, doi: 10.1016/j.earscirev.2018.06.011.

Niu, Y., Wilson, M., Humphreys, E.R., & O'Hara, M. (2011). The Origin of Intra-plate Ocean Island Basalts (OIB): the Lid Effect and its Geodynamic Implications. *Journal of Petrology*, *52*, 1443-1468, doi: 10.1093/petrology/egr030.

Nolasco, R., Tarits, P., Filloux, J.H., & Chave, A.D. (1998). Magnetotelluric imaging of the Society Islands hotspot. *Journal of Geophysical Research*, *103*, 30287-30309, doi: 10.1029/98JB02129.

Novella, D., Frost, D.J., Hauri, E.H., Bureau, H., Raepsaet, C., & Roberge, M. (2014). The distribution of H_2O between silicate melt and nominally anhydrous peridotite and the onset of hydrous melting in the deep upper mantle. *Earth and Planetary Science Letters*, *400*, 1-13, doi: 10.1016/j.epsl.2014.05.006.

O'Reilly, S.Y., & Griffin, W.L. (2010). The continental lithosphere–asthenosphere boundary: Can we sample it? *Lithos*, *120*, 1-13, doi: 10.1016/j.lithos.2010.03.016.

Parsons, B., & McKenzie, D. (1978). Mantle Convection and the Thermal Structure of the Plates. *Journal of Geophysical Research*, *83*, 4485-4496, doi: 10.1029/JB083iB09p04485.

Pilet, S., Baker, M.B., & Stolper, E.M. (2008). Metasomatized Lithosphere and the Origin of Alkaline Lavas. Science, 320, 916-919, doi: 10.1126/science.1156563.

Pilet, S., Abe, N., Rochat, L., Kaczmarek, M.-A., Hirano, N., Machida, S., Buchs, D.M., Baumgartner, P.O., & Müntener, O. (2016). Pre-subduction metasomatic enrichment of the oceanic lithosphere induced by plate flexure. *Nature Geoscience*, *9*, 898-903, doi: 10.1038/ngeo2825.

Priestley, K., McKenzie, D., & Ho, T. (2019). A Lithosphere–Asthenosphere Boundary—a Global Model Derived from Multimode Surface-Wave Tomography and

Petrology. In *Lithospheric Discontinuities* (Eds., H. Yuan and B. Romanowicz). doi:10.1002/9781119249740.ch6.

Prytulak, J., & Elliott, T. (2007). TiO_2 enrichment in ocean island basalts. *Earth and Planetary Science Letters*, *263*, 388-403, doi: 10.1016/j.epsl.2007.09.015.

Ringwood, A.E., Kesson, S.E., Hibberson, W., & Ware, N. (1992). Origin of kimberlites and related magmas. *Earth and Planetary Science Letters*, *113*, 521-538, doi: 10.1016/0012-821X(92)90129-J.

Rohrbach, A., & Schmidt, M.W. (2011). Redox freezing and melting in the Earth's deep mantle resulting from carbon-iron redox coupling. *Nature*, *472*, 209-212, doi: 10.1038/nature09899.

Rychert, C.A., Harmon, N., & Tharimena, S. (2020). Seismic Imaging of the Base of the Ocean Plates. In *Lithospheric Discontinuities* (Eds., H. Yuan and B. Romanowicz), doi: 10.1002/9781119249740.ch4.

Sarafian, E., Evans, R.L., Collins, J.A., Elsenbeck, J., Gaetani, G.A., Gaherty, J.B., Hirth, G., & Lizzarralde, D. (2015). The electrical structure of the central Pacific upper mantle constrained by the NoMelt experiment. *Geochemistry, Geophysics, Geosystems*, *16*, 1115-1132, doi: 10.1002/2014GC005709.

Sato, Y., Hirano, N., Machida, S., Yamamoto, J., Nakanishi, M., Ishii, T., Taki, A., Yasukawa, K., & Kato, Y. (2018). Direct ascent to the surface of asthenospheric magma in a region of convex lithospheric flexure. *International Geology Review*, *60*, 1231-1243, doi: 10.1080/00206814.2017.1379912.

Schmeling, H. (1986). Numerical models on the influence of partial melt on elastic, anelastic and electrical properties of rocks. Part II electrical conductivity. *Earth and Planetary Science Letters*, *43*, 123-136, doi: 10.1016/0031-9201(86)90080-4.

Schmerr, N. (2012). The Gutenberg Discontinuity: Melt at the Lithosphere-Asthenosphere Boundary. *Science*, *335*, 1480-1483, doi: 10.1126/science.1215433.

Schmidt, M.W., & Poli, S. (2014). 4.19 - Devolatilization During Subduction. In *Treatise on Geochemistry, Second Edition* (Eds., Heinrich D. Holland and Karl K. Turekian), 669-701, doi: 10.1016/B978-0-08-095975-7.00321-1.

Selway, K., O'Donnell, J.P., & Özaydin, S. (2019). Upper Mantle Melt Distribution From Petrologically Constrained Magnetotellurics. *Geochemistry, Geophysics, Geosystems*, *20*, 3328-3346, doi: 10.1029/2019GC008227.

Selway, K., & O'Donnell, J.P. (2019). A small, unextractable melt fraction as the cause for the low velocity zone. *Earth and Planetary Science Letters*, *517*, 117-124, doi: 10.1016/j.epsl.2019.04.012.

Shimizu, K., Ito, M., Chang, Q., Miyazaki, T., Ueki, K., Toyama, C., Senda, R., Vaglarov, B.S., Ishikawa, T., & Kimura J.-I. (2019). Identifying volatile mantle trend with the water–fluorine–cerium systematics of basaltic glass. *Chemical Geology*, *522*, 283-294, doi: 10.1016/j.chemgeo.2019.06.014.

Sifré, D., Hashim, L., & Gaillard, F. (2015). Effects of temperature, pressure and chemical compositions on the electrical conductivity of carbonated melts and its relationship with viscosity. *Chemical Geology*, *418*, 189-197, doi: 10.1016/j.chemgeo.2014.09.022.

Sifré, D., Gardés, E., Massuyeau, M., Hashim, L., Hier-Majumder, S., & Gaillard, F. (2014). Electrical conductivity during incipient melting in the oceanic low-velocity zone. *Nature*, *509*, 81-85, doi: 10.1038/nature13245.

Simonetti, A., & Neal, C.R. (2010). In-situ chemical, U-Pb dating, and Hf isotope investigation of megacrystic zircons, Malaita (Solomon Islands): Evidence for multi-stage alkaline magmatic activity beneath the Ontong Java Plateau. *Earth and Planetary Science Letters*, *295*, 251-261, doi: 10.1016/j.epsl.2010.04.004.

Smart, K.A., Tappe, S., Ishikawa, A., Pfänder, J.A., & Stracke, A. (2019). K-rich hydrous mantle lithosphere beneath the Ontong Java Plateau: Significance for the genesis of oceanic basalts and Archean continents. *Geochimica et Cosmochimica Acta*, *248*, 311-342.

Sobolev, A.V., Hofmann, A.W., Kuzmin, D.V., Yaxley, G.M., Arndt, N.T., Chung, S.-L., Danyushevsky, L.V., Elliott, T., Frey, F.A., Garcia, M.O., Gurenko, A.A., Kamenetsky, V.S., Kerr, A.C., Krivolutskaya, N.A., Matvienkov, V.V., Nikogosian, I.K., Rocholl, A., Sigurdsson, I.A., Sushchevskaya, N.M., & Teklay, M. (2007). The Amount of Recycled Crust in Sources of Mantle-Derived Melts. *Science*, *316*, 412-417, doi: 10.1126/science.1138113.

Soltanmohammadi, A., Grégoire, M., Rabinowicz, M., Gerbault, M., Ceuleneer, G., Rahgoshay, M., Bystricky, M., & Benoit, M. (2018). Transport of Volatile-rich Melt from the Mantle Transition Zone via Compaction Pockets: Implications for Mantle Metasomatism and the Origin of Alkaline Lavas in the Turkish–Iranian Plateau. *Journal of Petrology*, *59*, 2273-2310, doi: 10.1093/petrology/egy097.

Stagno, V., & Frost, D.J. (2010). Carbon speciation in the asthenosphere: Experimental measurements of the redox conditions at which carbonate-bearing melts coexist with graphite or diamond in peridotite assemblages. *Earth and Planetary Science Letters*, *300*, 72-84, doi: 10.1016/j.epsl.2010.09.038.

Stagno, V., Ojwang, D.O., McCammon, C.A., & Frost, D.J. (2013). The oxidation state of the mantle and the extraction of carbon from Earth's interior. *Nature*, *493*, 84-88, doi: 10.1038/nature11679.

Stamm, N., & Schmidt, M.W. (2017). Asthenospheric kimberlites: Volatile contents and bulk compositions at 7 GPa. *Earth and Planetary Science Letters*, *474*, 309-321, doi: 10.1016/j.epsl.2017.06.037.

Suetsugu, D., Shiobara, H., Sugioka, H., Ito, A., Isse, T., Kasaya, T., Tada, N., Baba, K., Abe, N., Hamano, Y., Tarits, P., Barriot, J.-P., & Reymond, D. (2012). TIARES Project—Tomographic investigation by seafloor array experiment for the Society hotspot. *Earth, Planets and Space*, *64*, 4 pp., doi: 10.5047/eps.2011.11.002.

Sun, C., Dasgupta, R. (2019). Slab–mantle interaction, carbon transport, and kimberlite generation in the deep upper mantle. *Earth and Planetary Science Letters*, *506*, 38-52, doi: 10.1016/j.epsl.2018.10.028.

Tada, N., Tarits, P., Baba, K., Utada, H., Kasaya, T., & Suetsugu, D. (2016). Electromagnetic evidence for volatile-rich upwelling beneath the society hotspot, French Polynesia. *Geophysical Research Letters*, *43*, 12021-12026, doi: 10.1002/2016GL071331.

Tappe, S., Foley, S.F., Stracke, A., Romer, R.L., Kjarsgaard, B.A., Heaman, L.M., & Joyce, N. (2007). Craton reactivation on the Labrador Sea margins: $^{40}Ar/^{39}Ar$ age and Sr–Nd–Hf–Pb isotope constraints from alkaline and carbonatite intrusives. *Earth and Planetary Science Letters*, *256*, 433-454, doi: 10.1016/j.epsl.2007.01.036.

Tappe, S., Pearson, D.G., Kjarsgaard, B.A., Nowell, G., & Dowall, D. (2013). Mantle transition zone input to kimberlite magmatism near a subduction zone: Origin of anomalous Nd–Hf isotope systematics at Lac de Gras, Canada. *Earth and Planetary Science Letters, 371-372*, 235-251, doi: 10.1016/j.epsl.2013.03.039.

Tappe, S., Smart, K.A., Stracke, A., Romer, R.L., Prelević, D, & van den Bogaard, P. (2016). Melt evolution beneath a rifted craton edge: 40Ar/39Ar geochronology and Sr–Nd–Hf–Pb isotope systematics of primitive alkaline basalts and lamprophyres from the SW Baltic Shield. Geochimica et Cosmochimica Acta, 173, 1-36, doi: 10.1016/j.gca.2015.10.006.

Tappe, S., Romer, R.L., Stracke, A., Steenfelt, A., Smart, K.A., Muehlenbachs, K., & Torsvik, T.H. (2017). Sources and mobility of carbonate melts beneath cratons, with implications for deep carbon cycling, metasomatism and riftinitiation. *Earth and Planetary Science Letters, 466*, 152-167, doi: 10.1016/j.epsl.2017.03.011.

Tappe, S., Smart, K., Torsvik, T., Massuyeau, M., & de Wit, M. (2018). Geodynamics of kimberlites on a cooling Earth: Clues to plate tectonic evolution and deep volatile cycles. *Earth and Planetary Science Letters, 484*, 1-14, doi: 10.1016/j.epsl.2017.12.013.

Tappe, S., Budde, G., Stracke, A., Wilson, A., & Kleine, T. (2020). The tungsten-182 record of kimberlites above the African superplume: Exploring links to the core-mantle boundary. *Earth and Planetary Science Letters, 547*, 14 pp., doi: 10.1016/j.epsl.2020.116473.

Tharimena, S., Rychert, C., Harmon, N., & White, P. (2017a). Imaging Pacific lithosphere seismic discontinuities—Insights from SS precursor modeling. *Journal of Geophysical Research: Solid Earth, 122*, 2131-2152, doi: 10.1002/2016JB013526.

Tharimena, S., Rychert, C., & Harmon, N. (2017b). A unified continental thickness from seismology and diamonds suggests a melt-defined plate. *Science, 357*, 580-583, doi: 10.1126/science.aan0741.

Tumiati, S., Fumagalli, P., Tiraboschi, C., & Poli, S. (2013). An Experimental Study on COH-bearing Peridotite up to 3·2GPa and Implications for Crust-Mantle Recycling. *Journal of Petrology, 54*, 453-479, doi: 10.1093/petrology/egs074.

van Keken, P.E., Hacker, B.R., Syracuse, E.M., & Abers, G.A. (2011). Subduction factory: 4. Depth-dependent flux of H_2O from subducting slabs worldwide. *Journal of Geophysical Research, 116*, 15 pp., doi: 10.1029/2010JB007922.

Wallace, M.L., & Green, D.H. (1988). An experimental determination of primary carbonatite magma composition. *Nature, 335*, 343-346, doi:10.1038/335343a0.

Wang, D., Mookherjee, M., Xu, Y., & Karato, S.-I. (2006). The effect of water on the electrical conductivity of olivine. *Nature, 443*, 977-980, doi: 10.1038/nature05256.

Weidendorfer, D., Schmidt, M.W., & Mattsson, H.B. (2017). A common origin of carbonatite magmas. *Geology, 45*, 4 pp., doi: 10.1130/G38801.1.

Weiss, Y., Griffin, W.L., Bell, D.R., & Navon, O. (2011). High-Mg carbonatitic melts in diamonds, kimberlites and the sub-continental lithosphere. *Earth and Planetary Science Letters, 309*, 337-347, doi: 10.1016/j.epsl.2011.07.012.

Yaxley, G.M., Berry, A.J., Rosenthal, A., Woodland, A.B., & Paterson, D. (2017). Redox preconditioning deep cratonic lithosphere for kimberlite genesis – evidence from the central Slave Craton. *Scientific Reports, 7*, 10 pp., doi: 10.1038/s41598-017-00049-3.

Zhang, G.-L., Chen, L.-H., Jackson, M. G., & Hofmann, A.W. (2017). Evolution of carbonated melt to alkali basalt in the South China Sea. *Nature Geoscience*, *10*, 229-235, doi: 10.1038/NGEO2877.

Figures

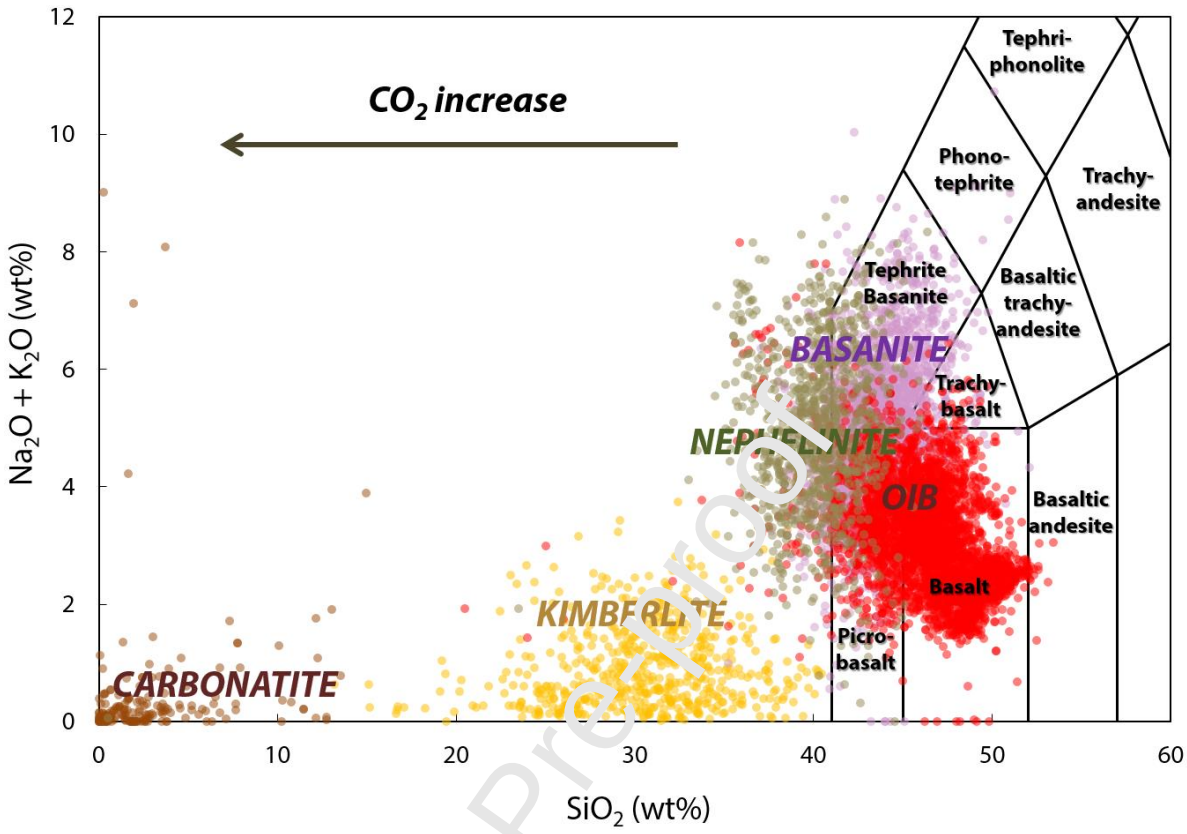

Fig. 1. Compositional range of natural intraplate melts, from low-SiO_2 carbonatitic melts to basaltic melts. Carbonatites (brown dots), nephelinites (green dots), basanites (purple dots) and OIBs (red dots) are selected from the GEOROC database (*http://georoc.mpch-mainz.gwdg.de/*). Kimberlites (yellow dots) are from the compilation of *Tappe et al. (2017; see their Supplementary File E and references therein)*. Lava compositions were selected from GEOROC database based on MgO content: carbonatites have MgO contents >12 wt% (and SiO_2 contents <15 wt% to remove anomalous outliers), while nephelinites, basanites and OIBs have MgO contents >8 wt% and <16 wt%.

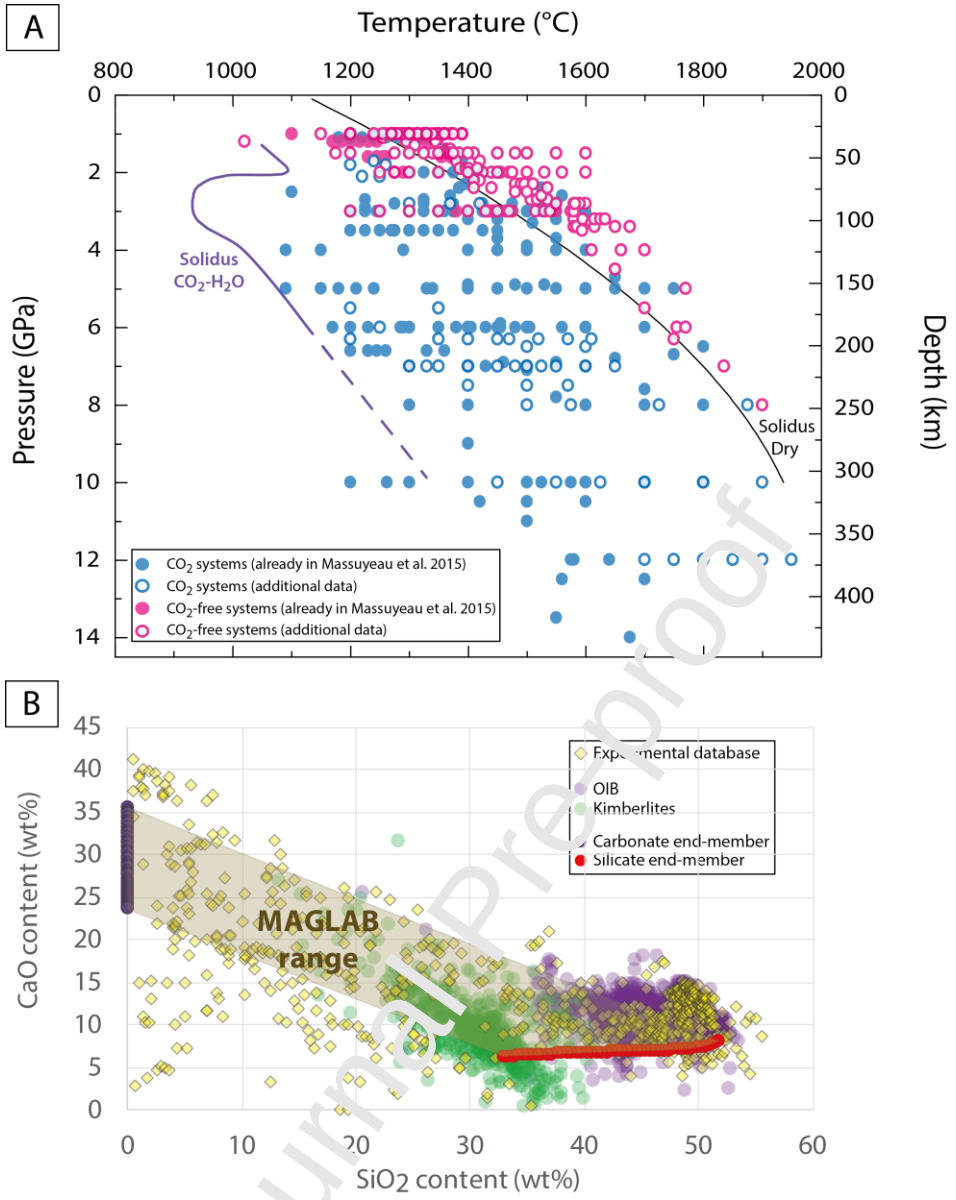

Fig. 2. Experimental database of melt compositions used for the calibration of MAGLAB. The description of the experimental database (i.e., pressure, temperature and composition space of melts) is presented in Table S3. All melts coexist with a typical mantle assemblage (i.e., saturated in olivine-opx±cpx±garnet/spinel). (A) Pressure/depth-temperature space. The data range from 1 to 14 GPa and from 1020 to 1950°C. Melting curves for different bulk peridotite conditions are also reported as a function of temperature and pressure/depth conditions (dry solidus from *Hirschmann (2000);* CO_2- and H_2O-bearing solidus from *Wallace and Green (1988)* from ~1 to ~4 GPa, and *Foley et al. (2009)* between 4 and 6 GPa, with extrapolation up to 10 GPa as shown by the dashed purple curve). (B) CaO-SiO_2 compositional space (see Fig. S3 for other major elements). The compositions of the silicate and carbonate melt end-members of our model are shown as red and purple circles, respectively. Combining these end-members yields compositions (light maroon shaded areas) covering a large proportion of the experimental database (yellow diamonds) as well as the chemical diversity of intraplate magmatism, from kimberlites to OIBs (green and light purple circles, respectively; see Fig. 1).

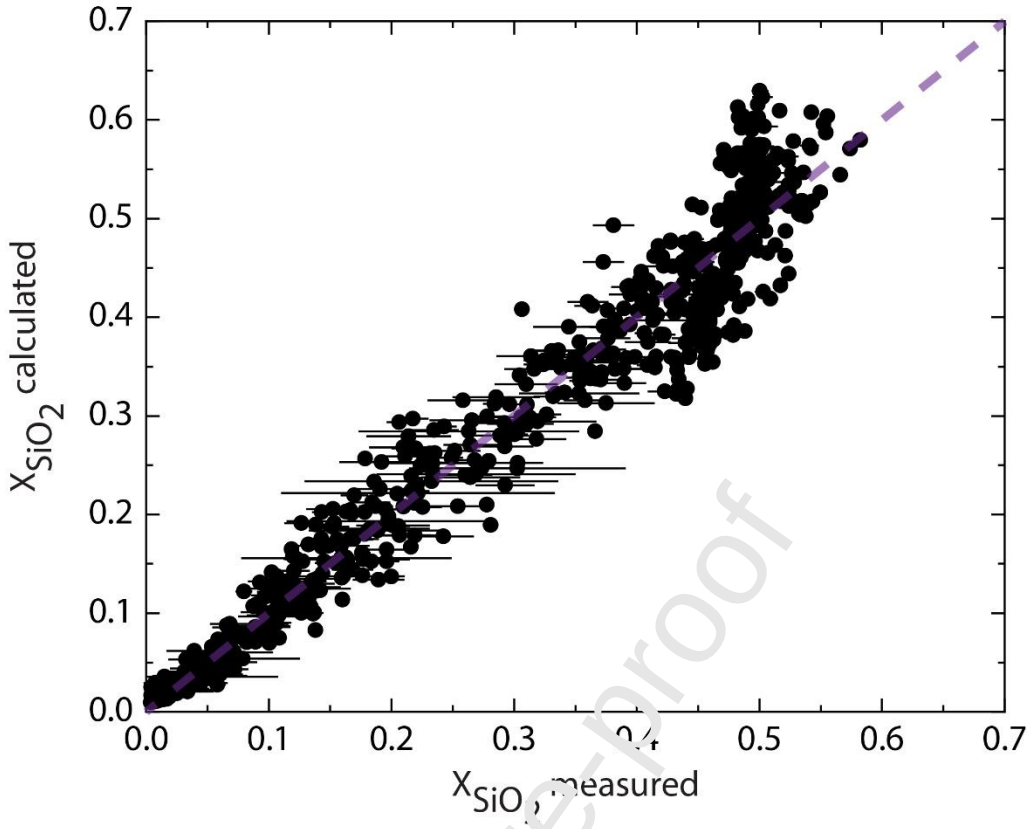

Fig. 3. Comparison of the molar fraction of SiO_2 in melt calculated with MAGLAB to that from the experimental database. The relative deviation of MAGLAB calculations, taken as $\frac{|x_{SiO_2}^{Melt} calculated - x_{SiO_2}^{Melt} measured|}{x_{SiO_2}^{Melt} measured}$, is ~15% on average.

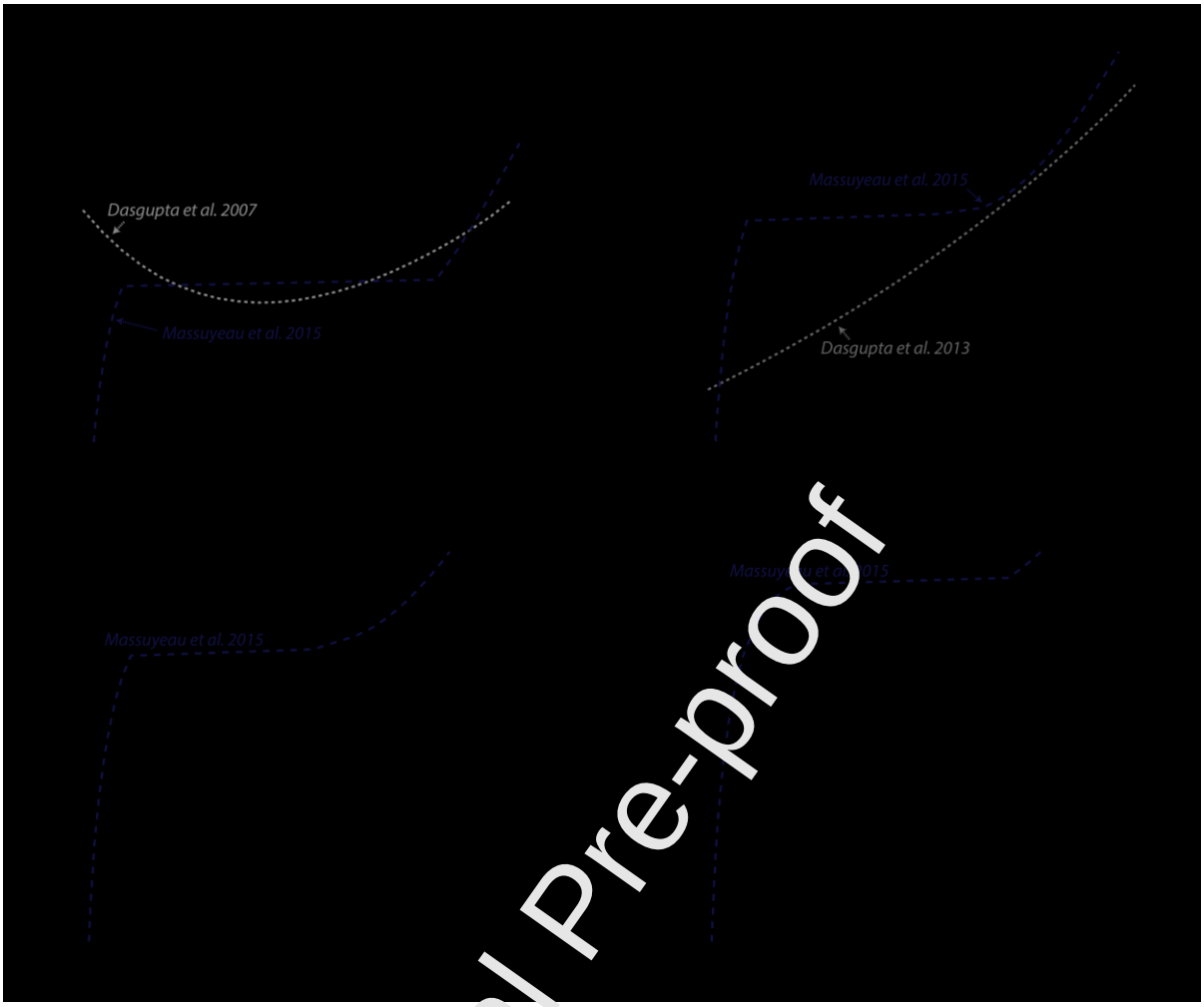

Fig. 4: Comparison of melt SiO_2 content calculated by MAGLAB with experimental data at (A) 3 GPa, (B) 5 GPa, (C) 7 GPa, and (D) 10 GPa. Also compared are the models of *Dasgupta et al. (2007)*, *Dasgupta et al. (2013)* and *Massuyeau et al. (2015)* in their pressure range of applicability (3 GPa, 5 GPa, and from ~2 to 10 GPa, respectively) at a bulk rock CO_2 content of 140 wt ppm (i.e., average mantle source; *Le Voyer et al., 2017*). Experimental melts reported here are H_2O-free, contain at least SiO_2, Al_2O_3, MgO, CaO, FeO and CO_2, and match pressure within ±0.5 GPa.

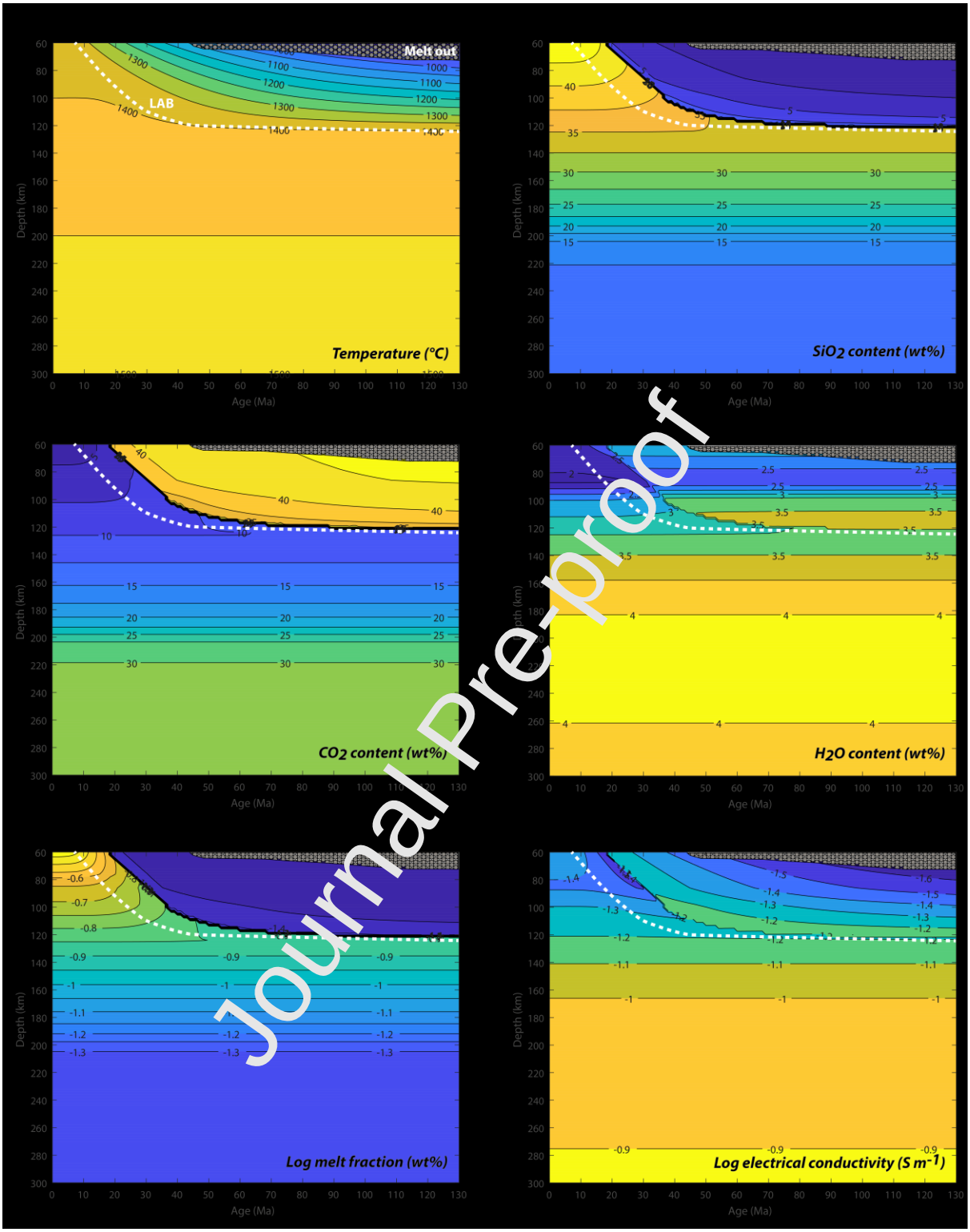

Fig. 5: Contours of MAGLAB equilibrium melt composition, melt fraction and electrical conductivity for oceanic upper mantle with average volatile content (140 wt ppm CO_2 – 240 wt ppm H_2O; *Le Voyer et al., 2017*) as a function of depth and age. (A) Mantle thermal structure with potential temperature T_P = 1350°C from *Grose and Afonso (2013)* (G13R1350 model). (B) SiO_2, (C) CO_2, and (D) H_2O contents of melts. (E) Melt fraction. (F) Bulk mantle electrical conductivity. The dotted grey areas (i.e., 'Melt out') at the top of each panel correspond to the subsolidus region *(Wallace and Green, 1988)*. The dashed white curve is an estimation of the LAB depth.

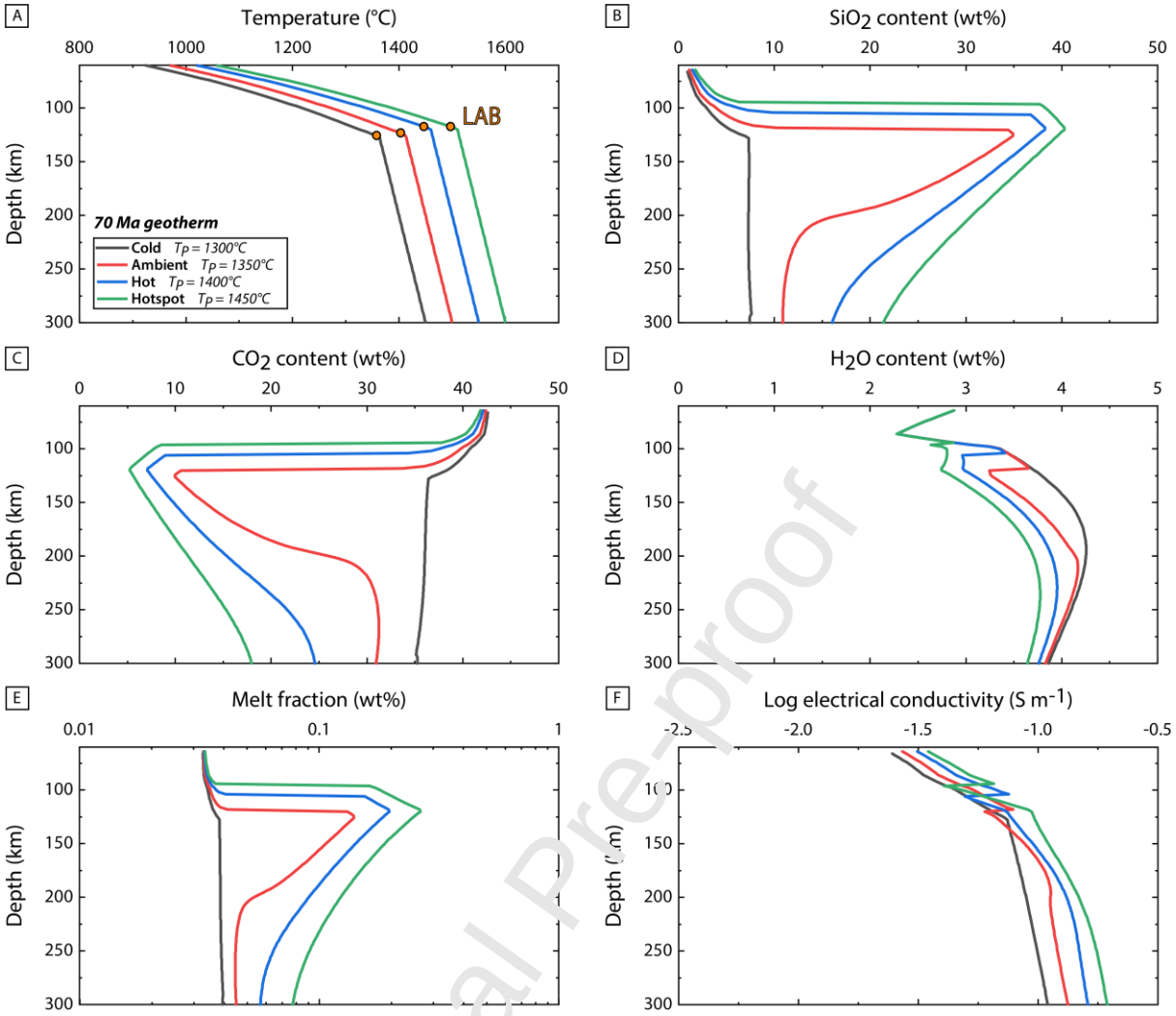

Fig. 6: MAGLAB equilibrium melt composition, melt fraction and electrical conductivity for oceanic upper mantle at 70 Ma as a function of depth and T_P, with average volatile content (140 wt ppm CO_2 – 240 wt ppm H_2O; *Le Voyer et al., 2017*). (A) Mantle thermal structures with potential temperature T_P = 1300, 1350, 1400 and 1450°C from *Grose and Afonso (2013)* (G13R1300, G13R1350, G13R1400, and G13R1450 models, respectively). (B) SiO_2, (C) CO_2, and (D) H_2O contents of melts. (E) Melt fraction. (F) Bulk mantle electrical conductivity. The orange circles in panel (A) provide an estimation of the LAB depth.

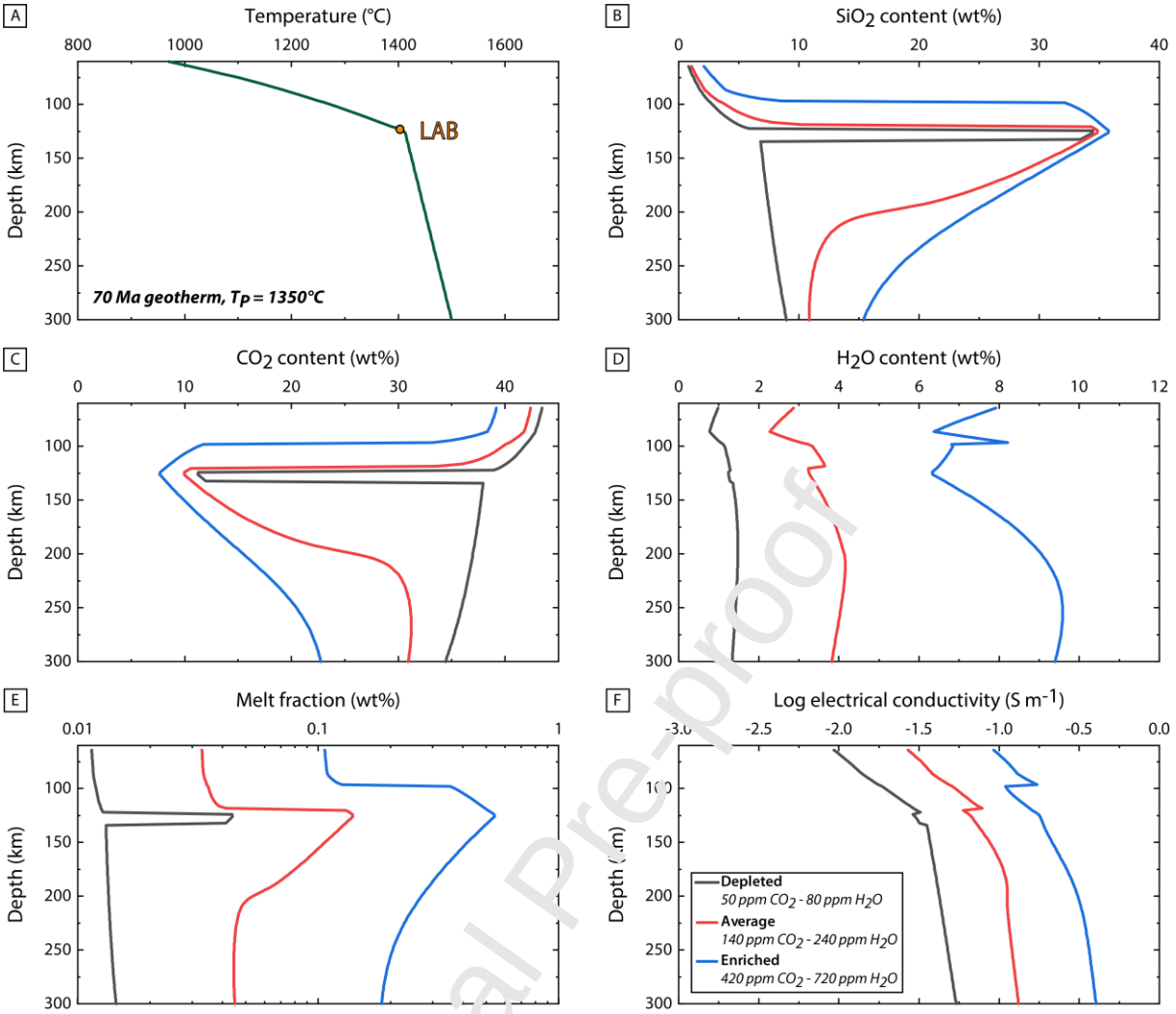

Fig. 7: MAGLAB equilibrium melt composition, melt fraction and electrical conductivity for oceanic upper mantle at 70 Ma with various volatile contents (50 wt ppm CO_2 – 80 wt ppm H_2O, 140 wt ppm CO_2 – 240 wt ppm H_2O, and 420 wt ppm CO_2 – 720 wt ppm H_2O) as a function of depth. (A) Mantle thermal structure with potential temperature T_P = 1350°C from *Grose and Afonso (2013)* (G13R1350 model). (B) SiO_2, (C) CO_2, and (D) H_2O contents of melts. (E) Melt fraction. (F) Bulk mantle electrical conductivity. The orange circle in panel (A) provides an estimation of the LAB depth.

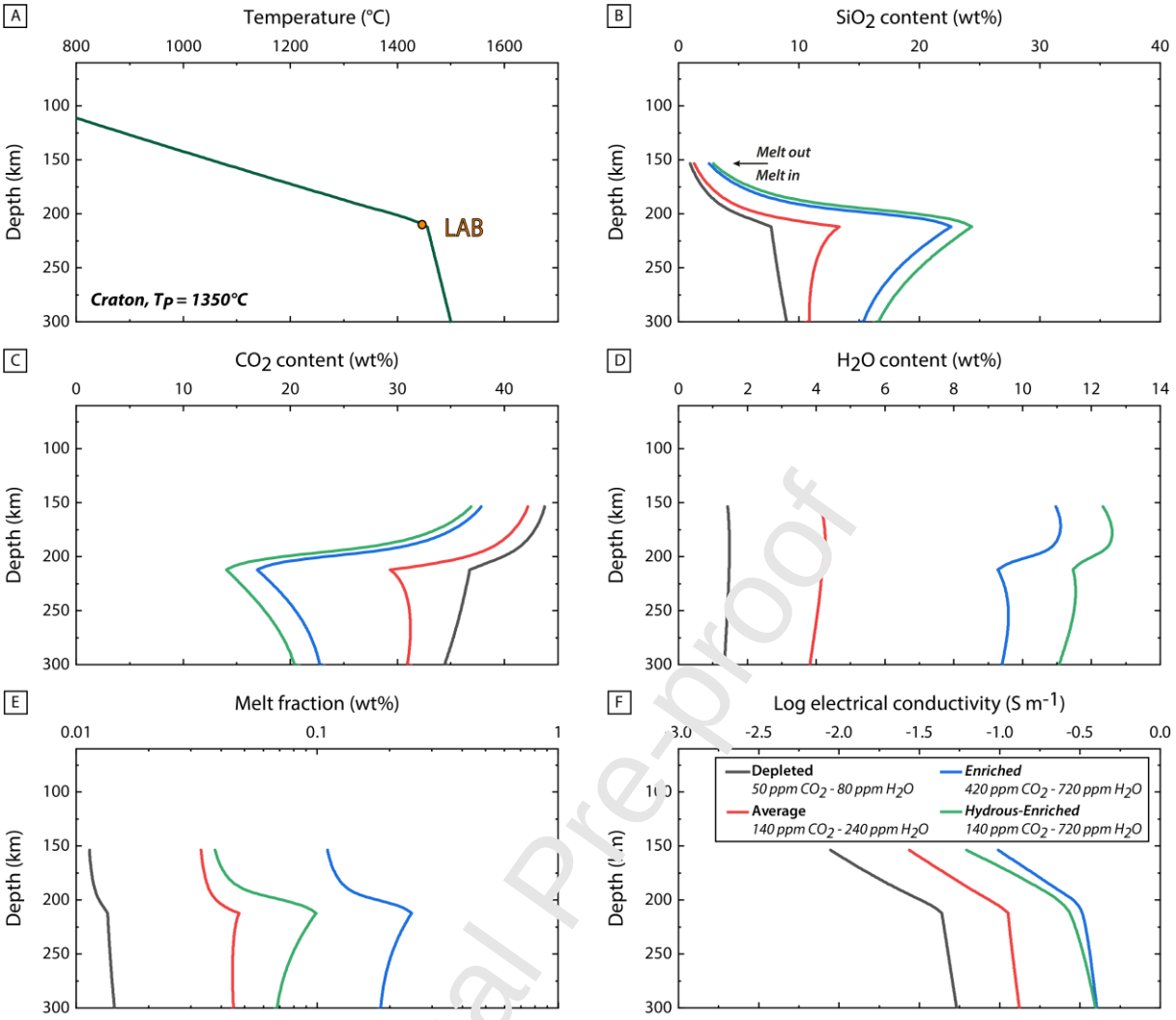

Fig. 8: MAGLAB equilibrium melt composition, melt fraction and electrical conductivity for cratonic upper mantle with various volatile contents (50 wt ppm CO_2 – 80 wt ppm H_2O, 140 wt ppm CO_2 – 240 wt ppm H_2O, 420 wt ppm CO_2 – 720 wt ppm H_2O, and 140 wt ppm CO_2 – 720 wt ppm H_2O) as a function of depth. (A) Mantle thermal structure with potential temperature T_P = 1350°C calculated with the numerical *FITPLOT* model *(McKenzie and Bickle, 1988; Matzen et al., 2011)* by fitting xenolith *P-T* array from a typical cratonic mantle (here, we consider the North Atlantic Craton beneath southern West Greenland; see more details in Fig. S6 and its caption). (B) SiO_2, (C) CO_2, and (D) H_2O contents of melts. (E) Melt fraction. (F) Bulk mantle electrical conductivity. The orange circle in panel (A) provides an estimation of the LAB depth. "Melt in" vs "Melt out" labels denote the depth at which mantle geotherm crosses the CO_2-H_2O-bearing peridotite solidus, and consequently delimits the top of the mantle melting zone; while the electrical conductivity calculations are performed by MAGLAB only for partially molten peridotite rocks, solid state mechanisms govern the mantle electrical conductivity in its shallow subsolidus portions.

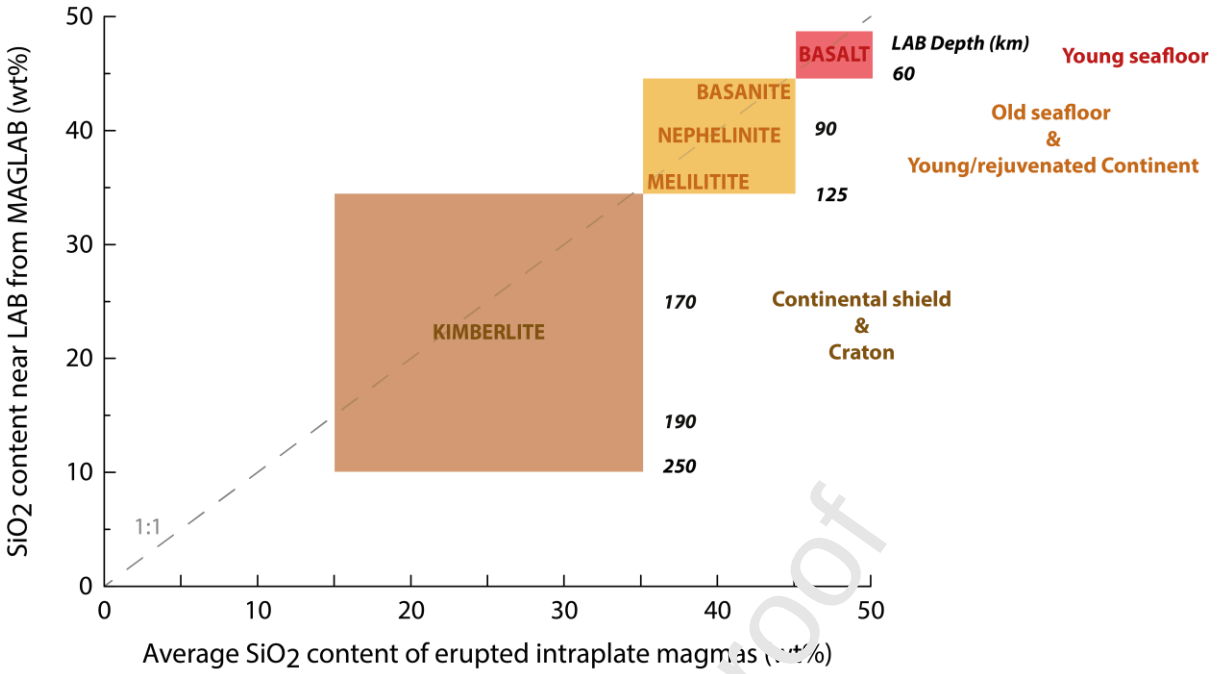

Fig. 9: Correspondence of the composition of intraplate magmas observed at the Earth's surface with the composition of primitive melts equilibrated at LAB depth calculated with MAGLAB. Different tectonic settings are considered: (i) Young seafloor (i.e., modern oceanic plate with age <10 Ma) with a LAB depth <~60 km; (ii) Old seafloor (i.e., modern oceanic plate with age >10 Ma) and Young/rejuvenated Continent, with a LAB depth between 60 and 125 km; (iii) Continental shield and Craton, with a LAB depth between 125 and 250 km. MAGLAB calculations are performed by varying the depth of the LAB as a function of the tectonic setting (see *P-T* conditions in Fig. S7), and considering a single average mantle source with 140 wt ppm CO_2 – 240 wt ppm H_2O *(Le Voyer et al., 2017)*. Similarly to the TAS diagram (e.g. Fig. 1), the melt SiO_2 content is here used as a proxy for the compositional range of intraplate magmas as found at the Earth's surface: 15-35 wt% for kimberlites, a progressive transition between 35 to 45 wt% from melilitite to nephelinite to basanite, and >45 wt% for regular basalts. Note OIB compositions as reported in Fig. 1 span basanitic to basaltic compositions.

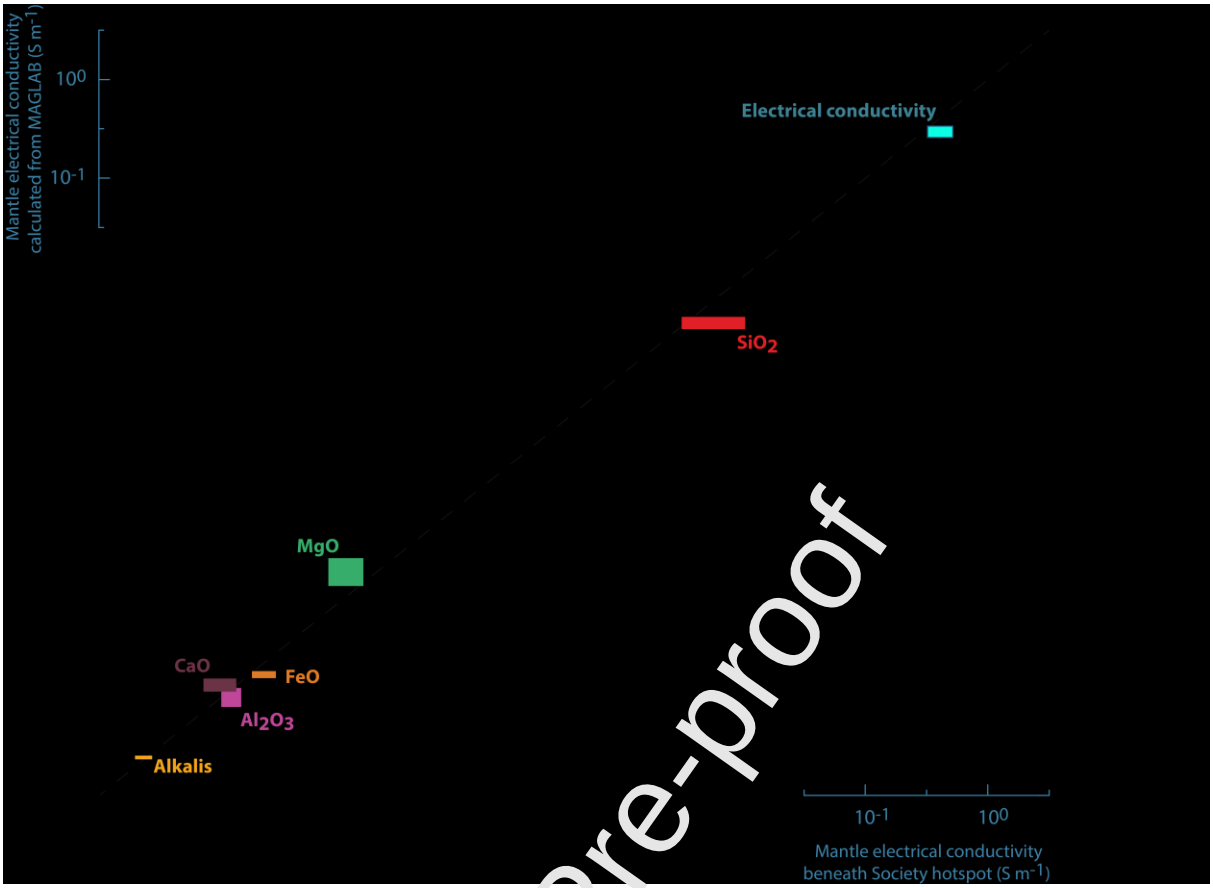

Fig. 10: Reproducing the petrological and electrical data at the LAB beneath Society hotspot (Pacific Ocean) using MAGLAB. Calculations are performed at LAB depth (120±10 km) according to the *P-T* conditions and mantle volatile content reported for the hotspot. The reported mantle potential temperature (T_p) is 1450°C (*Herzberg and Asimow, 2008*; mantle thermal structure simulated with GDH1450 model from *Grose and Afonso 2013*), and the mantle volatile content is ~700 wt ppm CO_2 and 720 wt ppm H_2O *(Aubaud et al., 2005)*. The average major element compositions of near-primary OIBs reported for the Society Islands are from *Dasgupta et al. (2010)*, on a volatile-free basis (also applied to the melt compositions from MAGLAB simulations). The high mantle electrical conductivities reported beneath Society hotspot are estimated within 110-130 km depth from the averaged 1-D electrical conductivities (*Tada et al. (2016)*; see also Fig. 11: "Anomaly Zone A, Society Islands").

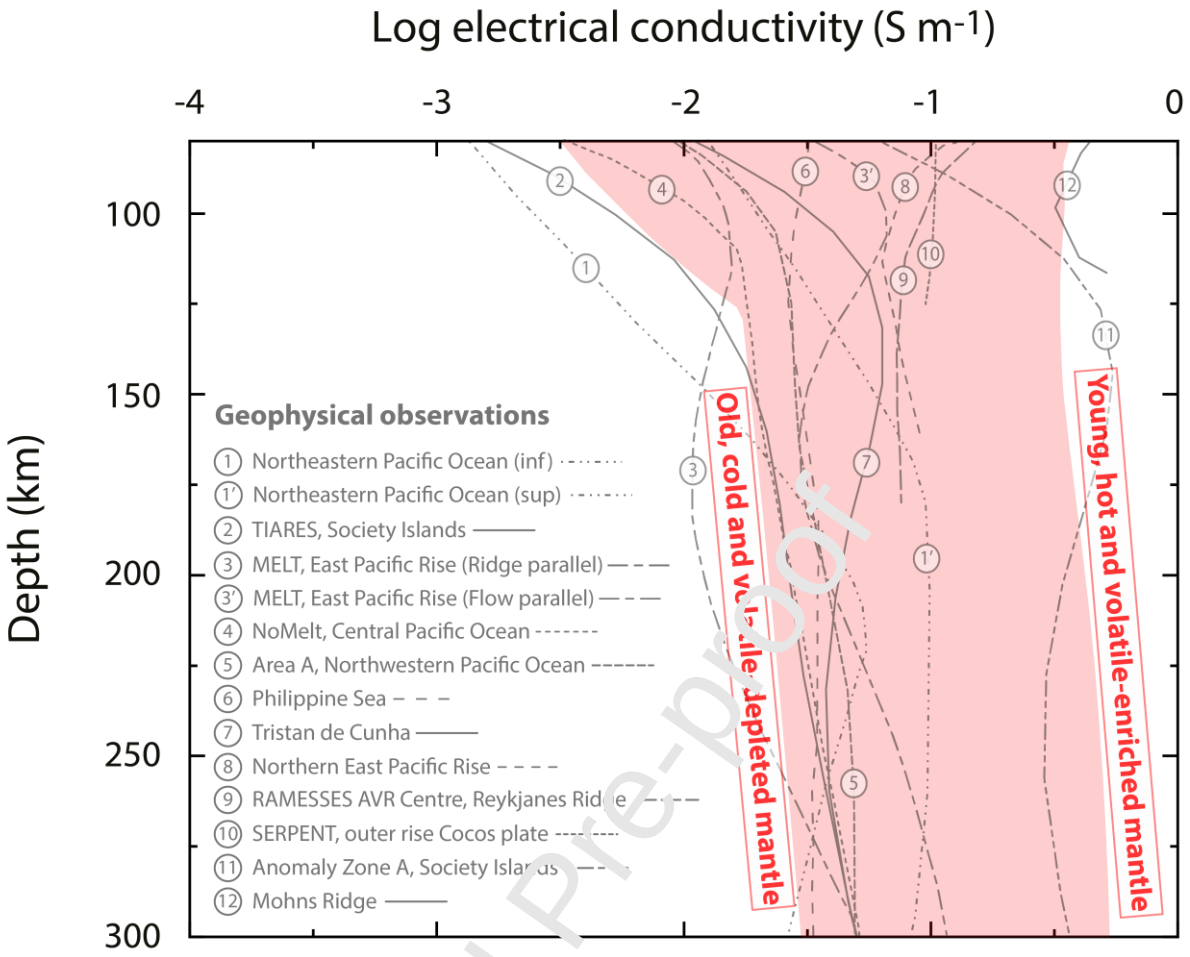

Fig. 11: Comparison between electrical profiles observed beneath various ocean floors and MAGLAB simulations. MAGLAB conductivities for partially molten peridotite rocks (light red area) range from (i) old, cold and highly depleted mantle (130 Ma, with T_P = 1300°C and 20 wt ppm CO_2 – 50 wt ppm H_2O) to (ii) young, hot and highly enriched mantle (0 Ma, with T_P = 1450°C and 700 wt ppm CO_2 – 720 wt ppm H_2O). The mantle thermal structures are G13R1300 and G13R1450 models from *Grose and Afonso (2013)*, with T_P = 1300°C and 1450°C, respectively. Electrical conductivity profiles of the oceanic upper mantle in dark grey are from various magnetotelluric studies. 1 and 1', conductivity profile in the northeastern Pacific Ocean between Hawaii and California *(Lizarralde et al., 1995)*. 2, Tomographic Investigation by seafloor ARray Experiment for the Society hotspot (TIARES) profile representing the 'background' mantle beneath the Society hotspot in the Pacific Ocean *(Tada et al., 2016)*. 3 and 3', Mantle Electromagnetic and Tomography (MELT) profile in the region of the East Pacific Rise *(Evans et al., 2005; Baba et al., 2006)*. 4, conductivity profile in the central Pacific Ocean ("NoMelt" experiment in *Sarafian et al., 2015)*. 5, conductivity profile in the northwestern Pacific Ocean ("Area A" in *Baba et al., 2013, 2017b*). 6, conductivity profile beneath the Philippine Sea *(Baba et al., 2010)*. 7, conductivity profile beneath the Tristan da Cunha hotspot in the southern Atlantic Ocean *(Baba et al., 2017a)*. 8, conductivity profile in the northern East Pacific Rise *(Key et al., 2013)*. 9, Reykjanes Axial Melt Experiment: Structural Synthesis from Electromagnetics and Seismics (RAMESSES) profile in the northern section of the Mid-Atlantic Ridge, i.e. the Reykjanes Ridge ("AVR Centre" in *Heinson et al., 2000*). 10, Serpentinite, Extension, and Regional Porosity Experiment across the Nicaragua Trench (SERPENT) profile beneath the outer rise of 22-24 Ma Cocos plate seafloor in the Pacific Ocean *(Naif et al., 2013; Naif, 2018)*. 11, conductivity

profile of a high-conductivity anomaly reported beneath the Society hotspot in the Pacific Ocean ("Zone A" in *Tada et al., 2016*). 12, conductivity profile beneath the Mohns Ridge ("3 Myr W" profile in *Johansen et al., 2019*).

No CRediT author statement. If this is mandatory, we will be pleased to provide it.

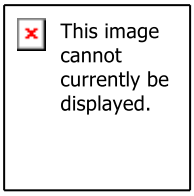

Highlights

- Combined petrology-geophysics inputs to model melting processes in the upper mantle
- Intraplate magma compositions relate to lithosphere thickness
- Quantification of melt fractions and CO_2-H_2O contents down to 300 km depth
- Heterogeneous mantle conductivities related to variable volatile contents